



Article

Multi-Scale Geophysical Methodologies Applied to Image Archaeological Ruins at Various Depths in Highly Terraneous Sites

Amin Ibrahim ¹, Khaled S. Gemal ¹ , Kamal Abdelrahman ^{2,*} , Naif Al-Otaibi ², Elkhedr Ibrahim ² and Saada A. Saada ³

- ¹ Environmental Geophysics Lab (ZEGL) at Geology Department, Faculty of Science, Zagazig University, Zagazig 44519, Egypt; dr_amin1983@zu.edu.eg (A.I.); Khaledgemal@zu.edu.eg (K.S.G.)
² Department of Geology and Geophysics, College of Science, King Saud University, Riyadh 11451, Saudi Arabia; nelotibee@KSU.EDU.SA (N.A.-O.); ebraheem@KSU.EDU.SA (E.I.)
³ Geology Department, Faculty of Science, Suez University, Suez 41522, Egypt; saada.elsayed@suezuniv.edu.eg
* Correspondence: khassanein@ksu.edu.sa

Abstract: Among all geophysical techniques, electrical resistivity and magnetic surveying as an integrative approach has been used widely for archaeological prospection at different scales of investigations. In this study, DC resistivity (1D vertical sounding and/2D/3D ERT) and magnetic surveys (total and gradient) as a multi-scale approach was applied in a highly terraneous archaeological site (Tell) with a case study to characterize and image the various archaeological assets at different depths with different spatial resolutions. Four critical zones of great interest within the considered Tell were surveyed. At the heart of the study area, three layers were depicted clearly from 1D resistivity sounding. A thick conductive zone of mostly clay is sandwiched between two resistive layers. The topmost layer contains construction debris (dated back to the Islamic Era), whereas the deeper layer could be related to Gezira sand on which the probable Pharaonic temple was constructed. A long 2D ERT profile using Wenner Beta (WB) and Dipole–Dipole (DD) arrays with a 5-m electrode spacing identified shallow high resistivity anomalies that could be related to construction ruins from fired bricks. Additionally, it succeeded in imaging the turtleback-shaped deeper resistive layer of mostly sand. At an elevated rim to the east and west of the Tell, total and vertical magnetic gradient maps clearly delineated different archaeological structures: the walls of the rooms of ancient Islamic settlers and the walls of water tanks from the Byzantine Era. Magnetic modeling assuming 2.5-dimensional magnetic models constrained by the 2D ERT inversion models could be used to create a realistic representation of the buried structures. Toward the northern part of the Tell, the joint application of the quasi-3D ERT inversion scheme and the magnetic survey revealed an anomaly of a well-defined geometric shape of an archaeological interest thought to be a crypt or water cistern based on nearby archaeological evidence. The overall results of the geophysical survey integrated with the image of some partially excavated parts provided the archaeologists with a comprehensive and realistic view of the subsurface antiquities at the study area.

Keywords: archaeological prospection; Electrical Resistivity Tomography (ERT); magnetic gradient; magnetic modeling (2.5D); multi-geophysical methodologies



Citation: Ibrahim, A.; Gemal, K.S.; Abdelrahman, K.; Al-Otaibi, N.; Ibrahim, E.; Saada, S.A. Multi-Scale Geophysical Methodologies Applied to Image Archaeological Ruins at Various Depths in Highly Terraneous Sites. *Remote Sens.* **2021**, *13*, 2055. <https://doi.org/10.3390/rs13112055>

Academic Editors: Gian Piero Deidda, Mahjoub Himi and Cassiani Giorgio

Received: 30 March 2021

Accepted: 19 May 2021

Published: 23 May 2021

Publisher's Note: MDPI stays neutral with regard to jurisdictional claims in published maps and institutional affiliations.



Copyright: © 2021 by the authors. Licensee MDPI, Basel, Switzerland. This article is an open access article distributed under the terms and conditions of the Creative Commons Attribution (CC BY) license (<https://creativecommons.org/licenses/by/4.0/>).

1. Introduction

The Tell Dibgou in the northeastern Nile Delta (Egypt) is a typical example (Figure 1) of a highly terraneous and multilayered archaeological settlement. The ancient topography and landscapes cannot create detailed and historically trustworthy sequential maps, due to a lack of attention to the archaeological stratigraphy of the territory [1,2] and the knowledge gap of the multiple archaeological structures at great depths. Keeping in mind that traditional large-scale archaeological excavations at great depths (>5 m) are very difficult due to

their invasive nature that destroys the subject of investigation [3–5]. In addition, the high cost and time consuming nature make the archaeological investigation of regional-scale and complex sites such as Tell Dibgou unsustainable.

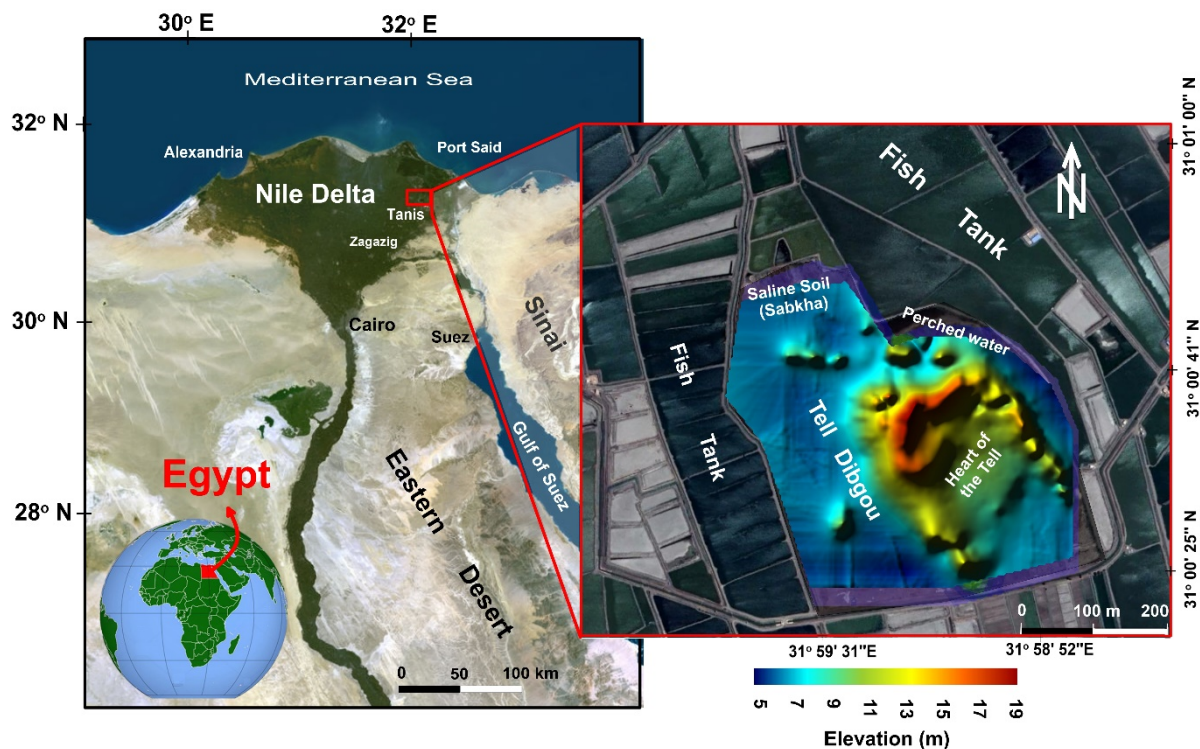


Figure 1. (Left) Google earth image displays the location of the Tell Dibgou archaeological settlement in the Nile Delta; and (Right) zoom-in relief map of the Tell and surrounding agricultural lands and fish tanks.

In such challenging cases, the role of geophysical surveys over large areas could be decisive to fill the knowledge gap and explore the buried targets at different depths with sufficient resolution. In addition, information about the location, depth, and dimensions of buried archaeological remains may be determined by means of geophysical investigation, which is carried out easily and quickly on the surface without disturbing or damaging the buried archaeological structures [6–15]. However, the manifestation of buried archaeological features in geophysical surveys is complex. The resolution of geophysical imaging and the ability to detect targets require a full understanding of the physical properties of materials in the subsurface, geophysical methods, and archaeological insights [16].

Practically, the multi-methodological geophysical approach can provide detailed information on the nature of the unseen archaeological targets where each geophysical survey responds to different earth properties [17]. In some cases, as in Tell Dibgou, the depths and the limited dimensions of archaeological features and the heterogeneities of near-surface materials, as well as some field and anthropic disturbances, may make it hard for a single method survey to delineate the spatial position and accurate dimensions of the archaeological remains due to the low value of signal-to-noise ratio (S/N) [17,18].

Thus, the use of multiple methods and different field techniques is good practice in most geophysical survey applications, including archaeogeophysical investigations. This increases the probability of success with at least one method and can greatly enhance interpretability [19]. As every geophysical technique responds to different physical properties, various datasets are complementary rather than redundant. As there are different scales of investigation, two different geophysical survey strategies can be adopted. In a small area (e.g., less than a hectare), undertaking a detailed survey of the whole area is more straightforward, whereas larger areas (e.g., Tell Dibgou) require some means of selecting areas for detailed surveys [20].

Geophysical surveys can often distinguish between artifact-laden and barren grounds and disclose important underground archaeological features (e.g., buried walls, tombs, obelisks, tunnels, water cisterns, ancient streets, and kilns). The presence of such archaeological features of notable size, typical of local architectures of antiquity, generates local anomalies, which can be clearly identified using an appropriate geophysical technique [21]. The combination of traditional archaeological excavations and geophysical imaging can lead to a comprehensive overview of the buried structures, the distribution of archaeological layers, and the properties of archaeological ruins [15,22,23]. However, the geophysical surveys are affected by uncertainties in interpreting the results, particularly if a lack of direct historical information on the surveyed site obscures historical activity at the site. Finally, present and historical structures at the site can generate and interfere with data quality, particularly in urban areas [24,25]. Therefore, strong collaborative partnerships between geophysicists who apply an empirical strategy for archaeological prospection and archaeologists who apply a conceptual strategy for prospection are beneficial. This interaction is important for a holistic understanding of an archaeological site. Furthermore, this can reduce the risk of encountering unexpected geological and site conditions (e.g., raising groundwater level) and consequently minimize delays and extra costs in subsequent work such as drilling or excavation.

Since 1946, geophysical techniques have been increasingly used with increasing rate in archaeological prospecting. The recent advances in geophysical data acquisition systems (2D/3D) and analysis software improve the applicability of multi-methodological approaches that can enhance the S/N ratio to improve the knowledge of the subsurface and visualization capabilities (2D/3D) for archaeological structures [17,26,27]. Electrical resistivity tomography (ERT), ground-penetrating radar (GPR), and magnetic methods are probably the most frequently applied methods in archaeological prospection [28–30]. Recently, passive seismic (i.e., microtremor) measurements are successfully applied in the investigation of ancient archaeological sites concerning the mapping of subtle and shallow sedimentary paleo-soils where other ordinarily used methods may fail or cannot be used [14]. Therefore, the combination of two or three techniques can provide the opportunity to gather significant information, producing excellent resolution images of many types of archaeological features located at different depths [9,30–36].

Magnetic survey is usually used in archaeological prospecting to detect features such as buried walls, pottery, bricks, fire pits, buried pathways, tombs, and numerous archaeological objects. These features are detected because they are more magnetic than the host materials [37,38]. In magnetic field survey, measurement of the total magnetic field (TMF) is widely used; however, the magnetic gradient is more effective in archaeological prospection [30,39,40]. In the same way, direct current resistivity (DCR) is one of the oldest methods in archaeological surveys. The recent development of the multi-electrode acquisition system has increased the ability of the DCR method for 2D/3D imaging and mapping complex geological and archaeological buried structures with a good spatial resolution [15,41–44]. The basic procedures and application of both methods in archaeological surveys, either individually or in combination, have been clearly described by several authors [7,16,28,35,45–48].

In the present work, Direct Current Resistivity (DCR) and magnetic methods (total field and vertical gradient) were employed in combination using different survey modes (1D/2D) to characterize the buried multiple archaeological structures at various depths in Tell Dibgou (Egypt). Both methods were implemented to check the likelihood of the presence of archaeological ruins at different depths and characterize the in situ archaeological stratigraphy to produce a more detailed settlement reconstruction. The selection of the applied methodologies depended on the main architectural structures found at Tell Dibgou, where the fired brick stones of high resistivity and magnetic susceptibility are dominant. To direct the future excavations to the areas indicated by geophysical surveys, the precise locations of geophysical measurements were recorded using Garmin GPS device. Here, data georeferencing was necessary for geophysical measurements to be associated with

each other and with direct field observations. This greatly facilitated the interpretation of geophysical data.

2. Site Description

Tell Dibgou is one of the largest ancient settlements in the northeastern Nile Delta, on the southern fringes of Manzala Lake, and covers 70 ha. It is located in UTM Zone 36 R between 401,908.86 and 402,976.95 Easting and 3,430,642.03 and 3,431,648.67 Northing. The site lies approximately 10 km northeast of Tell San El-Hagar, which contains the ruins of Tanis, the capital of Egypt during the 21st and 22nd dynasties (Figure 2).

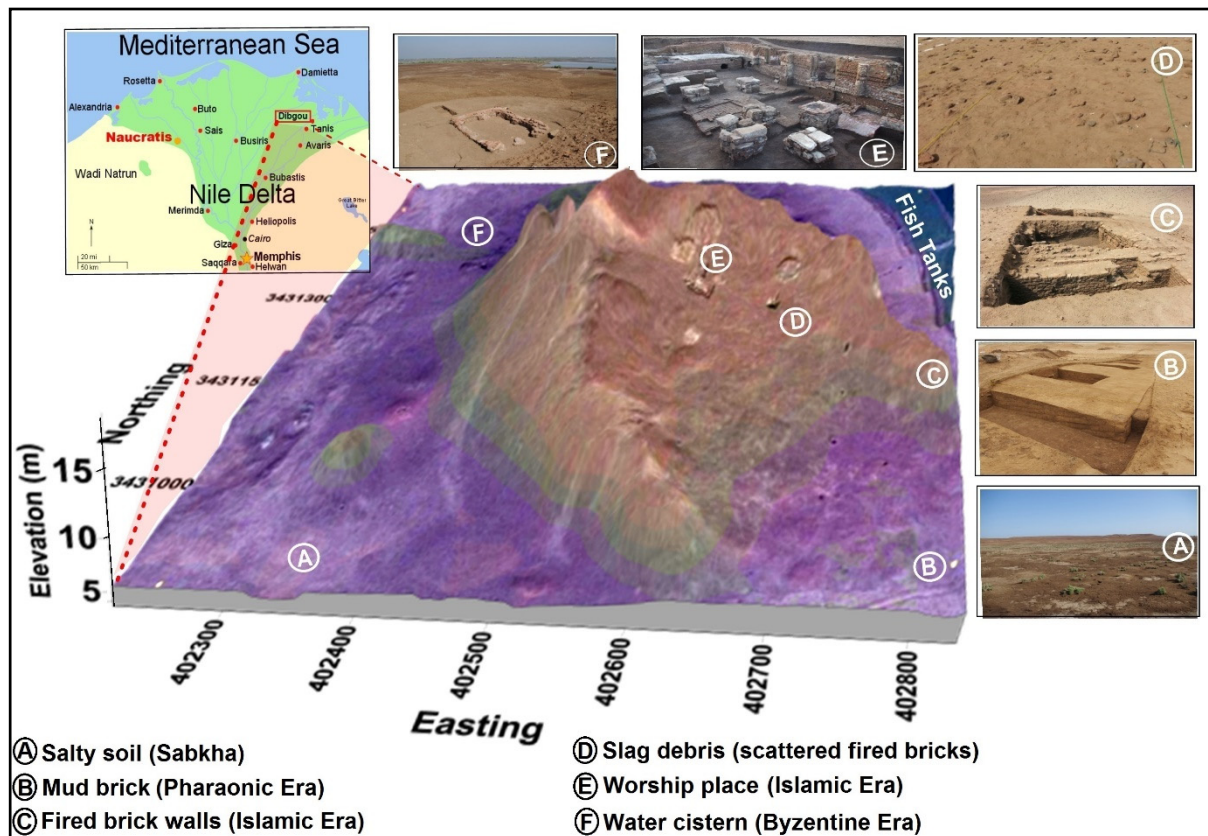


Figure 2. Map of the location, 3D topographic model, and different archaeological ruins of the Tell Dibgou archaeological site [49].

However, the archaeological site has not been fully investigated. It was first investigated during rescue excavations, completed by the Mission of Archaeology of Tell Dibgou (MATD), and has been under systematic excavation since 2014. The excavations were conducted before, during, and even after the geophysical survey. Besides these planned excavations, random digging by non-specialists and robber actions were recognized. Unfortunately, the ground conditions of Dibgou are generally uneven and covered with anthropogenic features represented by a dense scattering of fired brick and slag debris (Figure 2).

3. Geological and Archaeological Context

The geographic position of archaeological sites in the northeastern Nile Delta often results in various surrounding geoenvironmental conditions, such as drains, floodplains, and fluvio-marine marshes, agricultural activities, and soil salinization. At our site, this salinization occurs toward Manzala Lake. The most distinct geomorphologic units recognized in the northeastern Nile Delta are sand islands or “turtlebacks”, known locally as Gezira. The turtlebacks represent relics of Middle Pleistocene sands carried by the Pre Nile

River [50]. Some of these sand islands are hidden within or interfinger with Holocene floodplain mud [51]. Most have archaeological importance and are considered excellent sites for settlements that have remained above the annual Nile floods [52] during periods of human occupation.

The Tell Dibgou area contains Quaternary deltaic sediments [53] subject to periodic flooding. Hence, the deltaic clayey sediments dominating the site are affected strongly by salinization and salt efflorescence in the form of thin crusts and rather thin pans approximately 5 cm thick (Figure 2A). The moisture regime is associated with the redistribution of salts and gypsum in soils characterized by an oscillating shallow water table. This environment has been classified as a Sabkha [54] and can have a disastrous impact on buried archaeological ruins.

Human activity at the site is dated back to the Third Intermediate Period; includes the Saito-Persian period and the Ptolemaic, Roman, and Byzantine periods; and ended in the first centuries from the Muslim Era [49]. In the northern slopes of the Tell, where Roman and Byzantine ceramics were exposed, four cisterns (>2 m height) for water storage attributable to the Byzantine era were identified (Figure 2F). These water tanks were built of solidly cemented fired bricks and are installed in the middle of raw brick walls. In the southern and western parts of the site, pottery shards appear on the surface, all of which were arranged chronologically between the Third Intermediate Period and the Late Period. In addition, throughout the lower periphery of the Tell, many traces of raw brick constructions are visible on the surface of the ground owing to color differences. The excavations in this area revealed several occupation levels and yellow mud-brick walls (Figure 2B), similar to those found on the Tell San El-Hagar (Tanis) in the levels attributable to the Third Intermediate Period and the Late Period [49]. The ceramic material found in these areas dates from a period extending from the Third Intermediate Period to the beginning of the Saito Period.

4. Methodology

4.1. Survey Procedure and Field Setup

As the archaeological site of Tell Dibgou covers about 70 ha, the second geophysical field strategy (modified sampling strategy) was preferred. Four localities (A–D in Figure 3) of particular interest within Tell Dibgou were selected to focus on detailed geophysical investigations. These localities were chosen based on the recommendations of the archaeologists of the Mission of Archaeology of Tell Dibgou (MATD) working in the area during our field survey in September 2018. The geophysical surveys were intended to help plan excavations in forthcoming seasons. The criteria used by the archaeologists in recommending these localized areas were the archaeological history of Tell Dibgou, soil conditions, aerial photographic evidence, field observations, and analyses of topographic features. The heart of the Tell (the area around Spot A) was selected for the study to discover the ruins of a probable temple and characterize the turtleback or Gezira sand. The other three localities (B–D)—on elevated rims—were selected to image the enclosure, which surrounds the heart of the Tell. Geophysical data were collected over different consecutive periods from summer 2018 toward the end of 2019. In parallel with the geophysical measurements, the elevations and positions of the magnetic stations and electrodes were determined using Garmin GPS device as these were used during data interpretation. The location of the accomplished geophysical measurements (sounding points, 2D ERT profiles and magnetic grids) are depicted in Figure 3. Table 1 summarizes the geophysical survey measurements and field parameters of each investigated site.

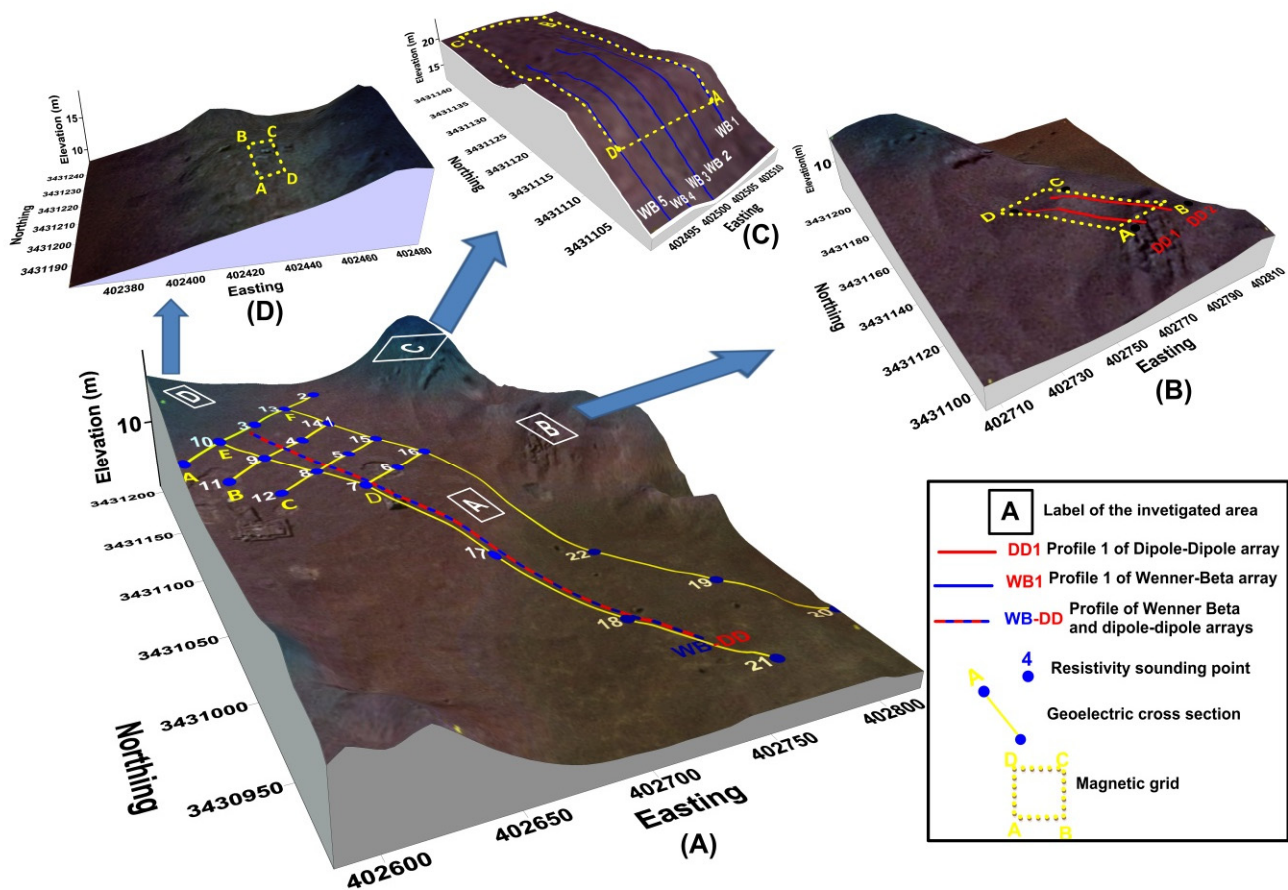


Figure 3. 3D surface maps of the investigated sites showing the geophysical survey layout: (A) heart of the Tell; (B) eastern periphery; (C) northeastern hill; and (D) western hill.

Table 1. The geophysical survey measurements and field parameters at all investigated sites.

Geophysical Surveys		Area of Investigation				
		Area (A)	Area (B)	Area (C)	Area (D)	
VES	Number of sounding points	22				
	Electrode array	WB	DD	DD	WB	
	Number of profiles	1	1	2	5	
	Profile length	235 m	235 m	30 m	30 m	
	2D ERT survey parameters	Number of electrodes	48	48	31	31
		Unit electrode separation (<i>a</i>)	5 m	5 m	1 & 2 m	1 m
		Depth levels (<i>n</i>)	7	15	6	9
		Number of measured data	360	332	492	675
Profile heading	NW-SE	NW-SE	NW-SE	S-N		
Magnetic Survey	Type of survey	—		Total and gradient	Total and gradient	Total Field
	Covered area	—		384 m ²	525 m ²	160 m ²
	Sampling interval	—		0.5 m	0.5 m	0.5 m
	Bottom sensor height	—		1.2 m	0.6 m	1.2 m
	Top sensor height	—		2.4 m	1.2 m	—
	Traverse heading	—		S-N	NW-SE	N-S

At the heart of Tell Dibgou (Figure 3A), the geophysical survey commenced by measuring 22 sounding points followed by long 2D ERT profile. The soundings were performed to provide a general overview of the multilayered archaeological settlements. Additionally, it helped us determine the optimal survey parameters for the subsequent 2D ERT profile (e.g., unit electrode separation (*a*) and depth levels (*n*)). The Schlumberger electrode array was selected because of its high penetration depth and lower sensitivity to lateral

inhomogeneity. The current electrode spacing ($AB/2$) varied between 1.5 and 100 m at each site.

The sounding points (blue dots in Figure 3A) were deployed along with two perpendicular sets of profiles marked by solid yellow lines. The first set encompassed four equidistant short profiles labeled A–D along straight lines in a southwest–northeast direction and typically spaced 25 m apart (Figure 3A). Each profile comprised between three and five VESs. The second set consisted only of two long profiles labeled E and F, and each one had seven VESs (Figure 3A). In this section, more attention was focused on two profiles; one of them is situated in the upper tip of Spot A and composed of five individual VESs, while the other crossed the middle part from north to south (Figure 3A). In addition to measuring the apparent resistivity data, the standard deviations (repeatability errors) were estimated to guide the processing and exclude some noise artifacts from the data.

A long 2D ERT profile was collected (235 m) to obtain a more resolved and detailed archaeological picture around Spot A. It was partially coincident with Profile D (Figure 3A). The red and blue colors indicate that the profile was measured using two types of electrode configurations: dipole–dipole (DD) and Wenner beta (WB). The survey parameters of DD and WB arrays are listed in Table 1. The measurement system employed in this study was multi-electrode system (48 electrodes) using the Siber instrument which operates automatically once the acquisition and geometrical parameters have been set. During the field measurements, the Siber (48) system obtained the apparent resistivity and calculated the standard deviation errors ($Q\%$) from repeat cycles. Measurements with $Q\%$ error of more than 5% were repeated or discarded.

The second area under investigation, around Spot B, is a small mound located at the eastern periphery of the investigated archaeological site (Figure 3B). The geophysical survey was organized and scheduled in the following steps. First, a magnetic survey in the form of a total magnetic intensity survey and a vertical magnetic gradient survey using two sensor separations, 0.5 and 1.2 m, were conducted. The magnetic profiles have a heading NNW–SSE and cover about 384 m^2 ($12\text{ m} \times 32\text{ m}$), the area marked by the dashed yellow rectangle (Figure 3B). The in-line and off-line distances were 0.5 and 1 m, respectively. The spatial resolution of the sampling was sufficient to detect archaeological structures down to a size of 1–0.5 m, and the aliased power fraction for the total field and vertical magnetic gradient was approximately zero, according to Reid [55] and Reynolds [56]. The magnetic profiles were measured in a zigzag traverse pattern (bidirectional survey). A base station was established and reoccupied every 15–20 min to monitor the temporal variations in the Earth's magnetic field. The intensity of the total magnetic field for the base station ranged between 43,925.8 and 43,968.8 nT during the magnetic survey of this site. Magnetic data were acquired using a well-known and robust Geometrics model G-856AX memory-mag proton precession magnetometer with 0.1-nT precision. Second, in October 2018, two 2D ERT lines were planned to follow up the results obtained from the inversion of magnetic data and separated by a 6-m distance. The two ERT profiles (P1 and P2), each with a length of 30 m and separated by 6 m (red lines, Figure 3B), were designed to be perpendicular to the prominent magnetic anomalies. The standard DD configuration was applied because of its sensitivity to lateral changes in resistivity and its better depth coverage at the ends of the lines [57]. Moreover, the DD configuration has a higher resolution in the shallow subsurface [58]. To improve the resolution for the DD array, particularly in noisy areas, we used overlapping data levels by combining measurements with different dipole lengths " a " ranging 1.0–2.0 m, whereas the " n " factor ranges 1–6.

The third area investigated, around Spot C, is located at the highest spur of the Tell (uplifted to approximately 20 m above sea level) in the northwestern part close to the former excavations (Figure 3C). The surveyed area occupies a rectangle of about 800 m², whose length is 40 m along the north and 20 m along the east. The importance of this area comes from the belief of the archaeologists who work in the Tell that the low relief adjacent to the investigated mound is the western gate of a probable temple. In summer 2019, geophysical investigations were conducted in two consecutive stages. First, magnetic measurements were in the form of total and vertical-gradient approaches. As the cultural layer is dominated by heterogeneous materials and relatively small archaeological targets, the sampling interval, line spacing, bottom sensor elevation, and sensor separation (the field survey parameters) were 0.5, 1, 0.6, and 0.6 m, respectively. The parameters were selected based on a trade-off between the area coverage and resolution. Second, ERT was executed in the form of a quasi-three-dimensional (3D) setup [15,59–61], where five parallel lines heading south–north (Figure 3C) were acquired in a profile mode using the WB configuration because it has been used commonly in the imaging of different archaeological prospections [15,62] and characterized by a high signal-to-noise ratio [63]. Additionally, it provides a good vertical resolution, which means that the depth to the base of archaeological targets can be detected well. Each traverse line has 31 electrode positions with minimum electrode spacing of 1 m. The nine depth levels of an interval of 1 m yielded 135 data points for each section. The mutual distance between adjacent traverses was 2 m (twice the in-line electrode spacing) to reduce the near-surface banded anomalies along the axis of the survey grid [15,57,64,65]. The 2D dataset measured were collated to create a single 3D ERT dataset with 675 data points. The geographic location (Easting and Northing) and elevation of each electrode position in the 2D ERT layout were gathered. The acquisition geometry for 3D geoelectrical resistivity imaging reduces not only the total number of measured data points but also the time and effort required for 3D resistivity surveying.

The last area under investigation is around Spot D, covered by a survey rectangle (8 m × 20 m) located in the western side of the area (Figure 3D), behind the periphery enclosing the heart of the Tell. Magnetic measurements in the form of the total magnetic field were acquired in the bidirectional mode along parallel paths 1 m apart, with a sampling interval of 0.5 m, to avoid spatial aliasing and image the expected small targets. The magnetometer sensor is at a nominal height of 2.4 m to avoid surface clutter and randomly distributed highly magnetic stones in the topmost layers.

4.2. Data Processing and Inversion

By examining the field sounding curves, we observed some minor and significant cusps, especially at Soundings 7 and 8 (Figure 4A). The upward cusp at Sounding 7 means that the current electrode crosses from low to high resistivity. In contrast, Sounding 8 shows a downward pointing cusp (i.e., the current electrode crosses from high to low resistivity). Most cusps in the measured one-dimensional (1D) sounding were pronounced at short current electrode spacings ($AB/2 = 1.5$ and 3 m) and caused mostly by small lateral inhomogeneities (slag debris and scattered fired bricks) close to the Earth surface. The measured sounding curves were processed, analyzed, and combined using the IPI2WIN program [66]. The apparent resistivity and $AB/2$ values are input and inverted using a 1D-based algorithm to estimate the true resistivities and thicknesses of the assumed horizontal layers. In this inversion scheme, the resistivity data along the profile were treated as a unit considering the lateral layering distribution rather than separate points [66]. The data points that had standard deviations of more than 5% (spikes) were excluded. During the inversion procedures, we considered the principle of equivalence, which states that a resistivity curve may be caused by many equivalent models [67,68]. The true model that best reflects the actual archaeological setting was built based on the excavation findings that were integrated during inversion by fixing the layer parameters (depth and resistivity).

The 2D resistivity profiles were processed and inverted using the commercial software RES2DINV, Ver 4.08 by Geotomo software, based on the least-squares inversion of Loke and Barker [69]. The inversion process was commenced by removing bad points from the dataset based on the percentage of standard deviation (Figure 4B). Moreover, the data errors were estimated and the elevation of the electrodes were considered and incorporated into the inversion subroutine. The robust inversion scheme (L1 norm) was applied because it was less sensitive to spurious outliers (noisy data points), which corrupt the resulting inversion model. Furthermore, it produces anomalies with regular and sharp boundaries compared with the least squares (L2) smoothness constraint. The constraint cutoff factor was selected to be 0.05 and sometimes 0.1 to reduce the effect of data points having a misfit between the measured and calculated apparent resistivities greater than 5%. The data show normal random noise, as evidenced by the exponential decrease in the number of data points with increasing data misfit (Figure 4C), as well as the clustering and alignment of most measured and calculated resistivity data along a close trend on a 45° line (Figure 4D). The low noise level and superiority of the data quality were manifested by the lower value of the root mean square (RMS = 5.61%), as shown in Figure 4D.

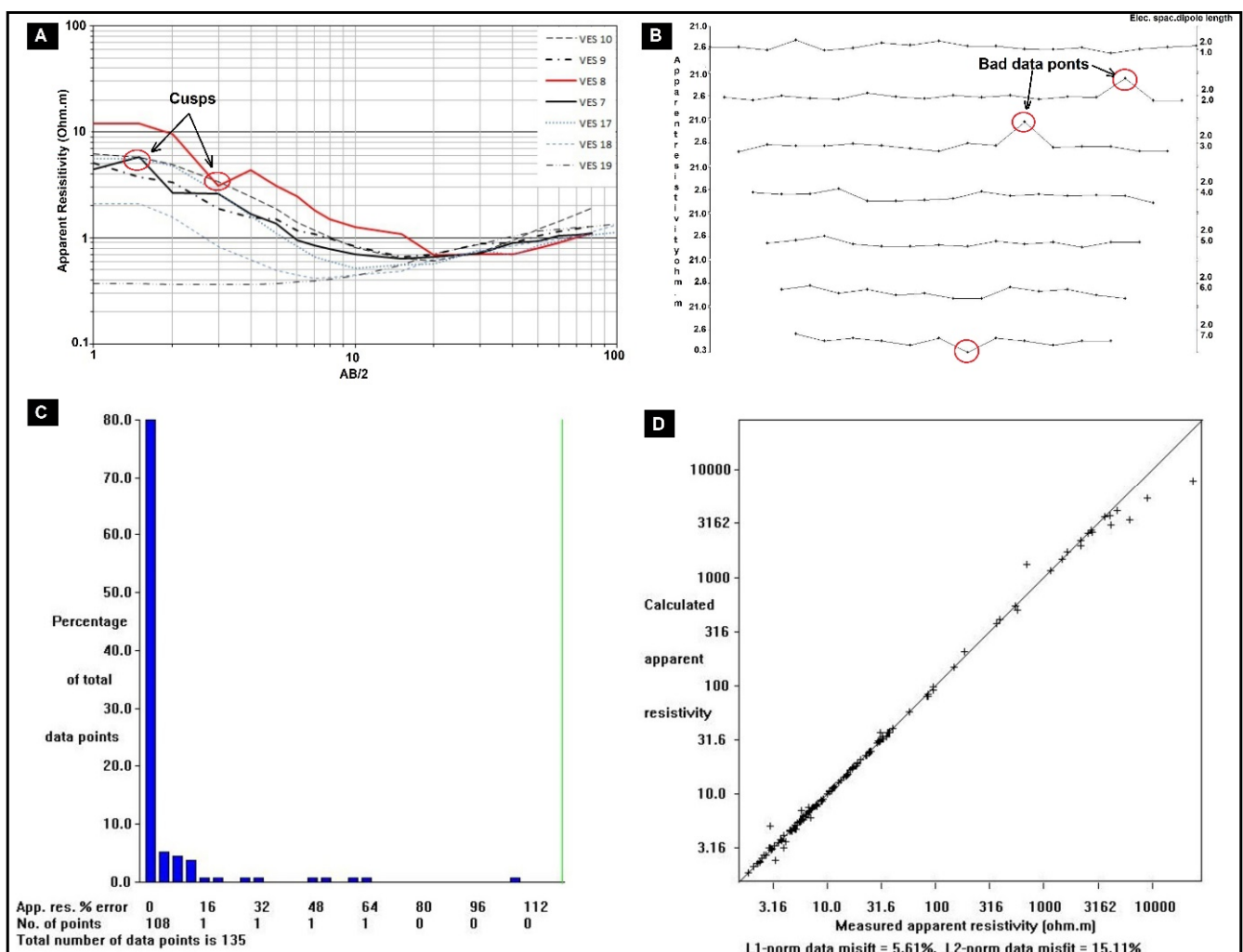


Figure 4. Examples of the measured resistivity data: (A) resistivity sounding points plotted on a bilogarithmic paper; (B) outliers in the 2D ERT profile; and (C,D) statistical plots of the misfit between the observed and calculated apparent resistivity values in the form of a bar chart and a scatterplot, respectively.

All 2D profiles were rearranged to produce a single 3D volume of apparent resistivity data. A full 3D inversion program of RES3DINV (ver. 3.14) was used to reconstruct the 3D resistivity variation [69,70]. Inversion parameters were adjusted for the measured data. A higher initial damping factor for the uppermost layers ($\lambda = 0.15$) and a diagonal roughness filter were used to reduce the banding effects [71], because the normal horizontal roughness filter tends to produce structures aligned along the x - and y -directions [70]. Because the topographic correction is necessary, the finite-element method was used to take into account the topographic effect on the distribution of equi-potential surfaces, hence correcting the measured potential difference, which is used to calculate the theoretical apparent resistivity values.

The acquired magnetic data are adversely impacted by noise, which makes interpretation difficult. The spikes (extraneous values) in the measurements were removed manually in a despiking process. Thereafter, the data were interpolated using the bidirectional gridding method because it can improve trends crossing the traversing direction [72]. Small-scale systematic errors manifested by chevron or zigzag patterns were removed using a lag correction. In addition, some grids may show a series of stripes oriented in the traverse direction. This effect is known as “traverse stripping” and is caused by a slight difference in the background level of alternating traverses. A heading correction or zero mean traverse correction could reduce this effect substantially. In addition, the mismatch between adjacent survey grids (grid edge discontinuities) was perceptible, so the application of the zero mean grid was required to correct this. Standard diurnal drift correction was accomplished by interpolating the drift derived from a base station magnetometer. Although the aforementioned processing steps removed a significant part of systematic error, a close examination of the magnetic maps revealed that the data were still affected by small-scale systematic noise (horizontal and vertical stripping patterns). Thereby, the leveling process was applied to remove this noncoherent residual error. The magnetic data were decorrugated using a grid-based technique known as the empirical leveling approach (microleveling). The International Geomagnetic Reference Field of the investigated area was removed from the diurnally corrected magnetic data using the 11th Generation, revised (2015). A reduction to North Pole (RTP) was implemented, under the assumption of inducing magnetization, to phase rotate the magnetic anomalies into their correct positioning. Most of the centers of the anomalies shifted northward by as much as 3 m, suggesting that the archaeological targets were magnetized by induction only (no remanent magnetization). Finally, prior to performing residualization and derivative-based techniques, a low-pass Butterworth filter was applied using a central wavelength of 0.63 m to smear out the spikes with high wavenumber components and large amplitude attributed to surface noise (e.g., scattered slag debris of fired bricks). The corrected magnetic data were enhanced and then plotted using the Oasis Montaj Program v.8.3 [72]. Figure 5 provides the efficiency of the applied sequential processing steps at two examples of magnetic datasets. Figure 5A,B shows the original and processed magnetic images of the area around spot B, respectively. In contrast, Figure 5C, D displays the raw and processed magnetic images of the area around spot C, respectively. All the magnetic data were plotted in color-shaded relief images to accentuate the archaeological features (Figure 5).

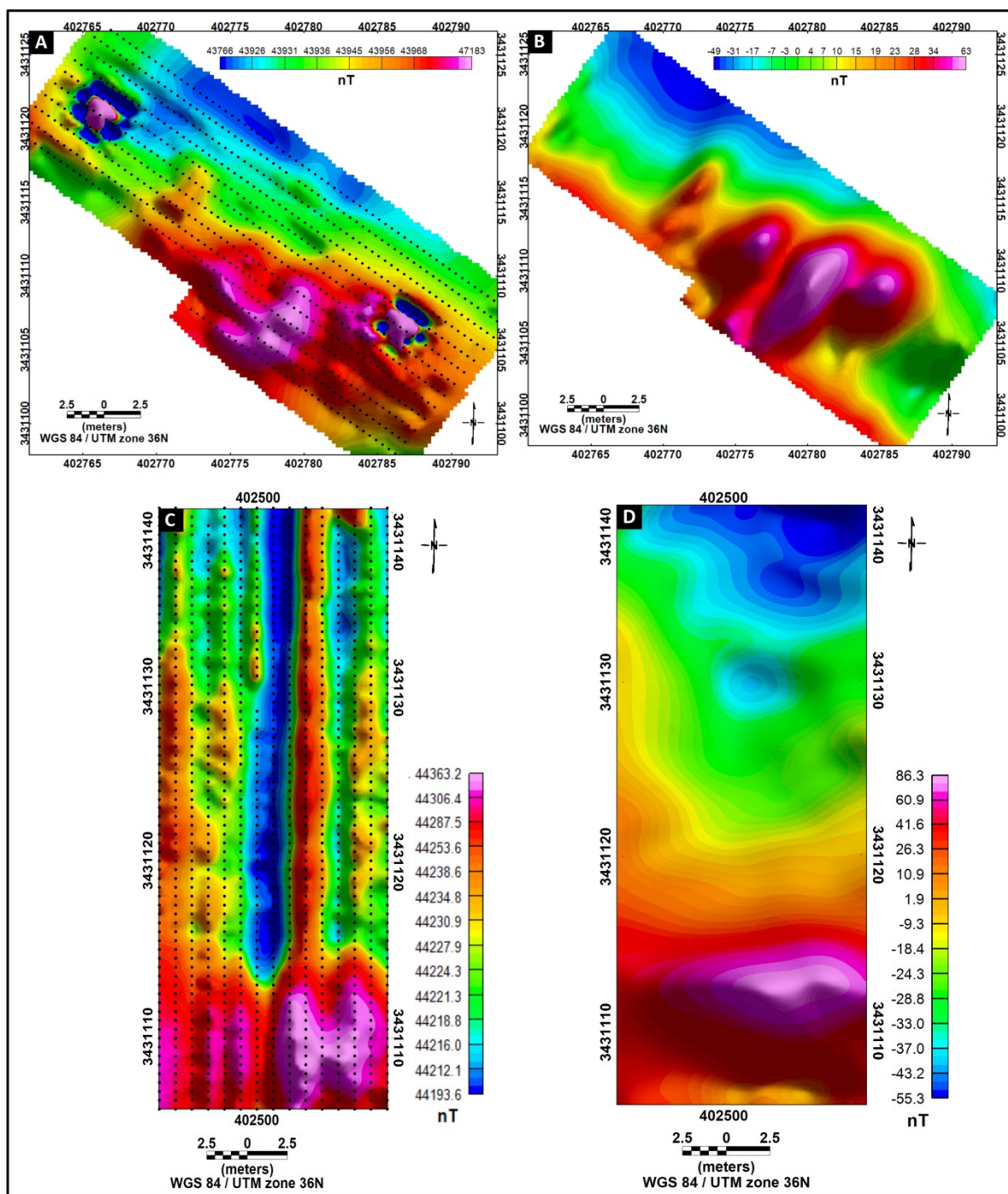


Figure 5. Examples of magnetic data processing: (A,B) original and processed magnetic maps at Site B, respectively; and (C,D) original and processed magnetic maps at Site C, respectively.

5. Results and Discussion

This section describes the results obtained by processing the dc resistivity and magnetic data. Overall, about 2.5 ha of the Dibgou site were surveyed. In particular, areas around Spots B and C were investigated using both magnetic (total and gradient-based approaches) and ERT methods. In contrast, in areas around Spots A and D, only resistivity (VES and 2D ERT) and magnetic (total field) methods were used, respectively. Fortunately, excavations were conducted by the MATD after the geophysical survey, which enabled the correlation of the geophysical and excavation results. The results for each surveyed area are presented and discussed independently in the following sections.

5.1. Area Around Spot A

Resistivity cross-sections derived from inverting the sounding points using a layered model were constructed in the form of a fence diagram to trace the archaeological layers in the heart of the Tell (Profile A is to the left and Profile E runs from left to right; Figure 6). An analysis of the constructed sections shows a multilayer model consisting of three layers. The first layer is characterized by a set of relatively high, dispersed resistivity values ($>7 \Omega \cdot \text{m}$) compared with an underlain highly conductive layer ($<1 \Omega \cdot \text{m}$). The surface layer is thicker in the higher area to the left, but it disappears downward in the lowland peripheries to the right of VES 18 (Figure 6). This layer was later confirmed to be composed of construction materials employed by ancient Islamic settlers, for example, fired brick walls mixed with an accumulation of slag debris and scattered bricks, consistent with the high-resistivity values. As deduced from resistivity sections, the thickness of this archaeological layer ranged between 2 and 3 m, mainly in good agreement with archaeological excavations. The second geoelectric layer, characterized by very low-resistivity values, is interpreted as salty clay deposits saturated with irrigation and seepage water from nearby fish tanks in the lowlands. The thickness of this layer is approximately 10 m and decreases gradually to the extreme left and right (Figure 6). The basal geoelectric layer is characterized by anomalous increasing in resistivity values ($>10 \Omega \cdot \text{m}$) at sounding Points 1, 3, and 10 in the heart of the Tell (Figure 6) which may indicate the appearance of Gezira sand layer below 10 m depth.

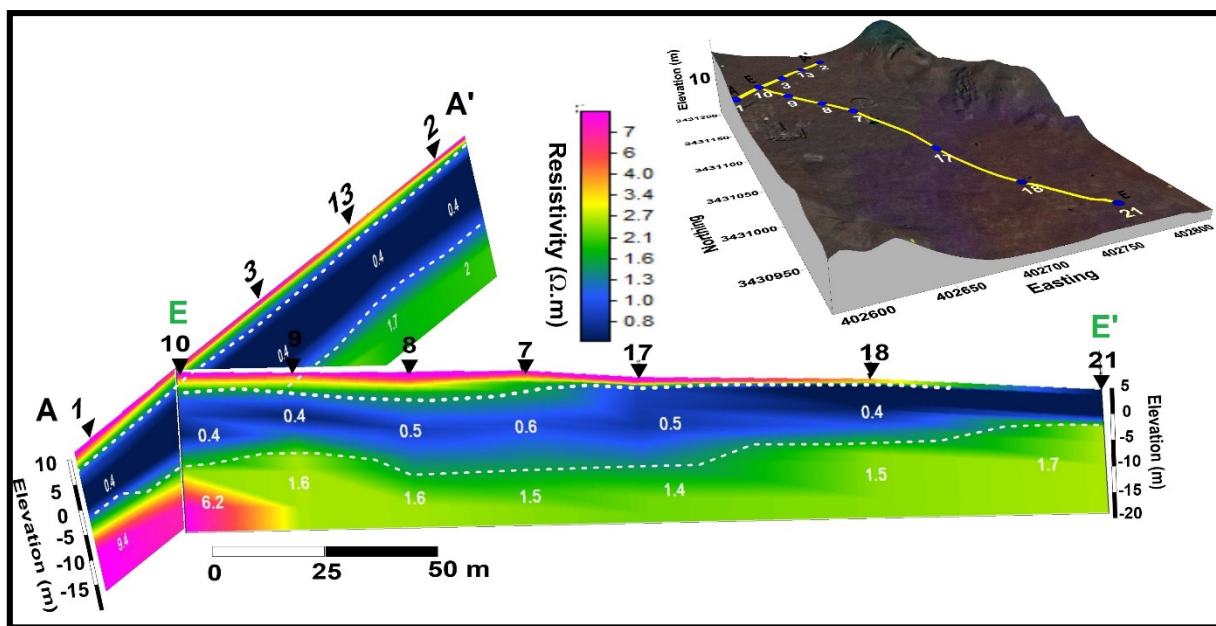


Figure 6. Fence diagram of resistivity cross-sections; white dashed lines represent archaeological layer boundaries, and the values are true resistivities.

The resistivity-depth model (Figure 6) along the SW–NE and SE–NW profiles shows many important features for understanding the distribution of multilayered archaeological settlements in the investigated site. However, the dimensions and orientations of the walls in the upper archaeological layer are not observed with clear boundaries in the layered or 1D resistivity dataset. This is probably because of the dense distribution of walls in the heart of the Tell and the spacing of the soundings. Moreover, an assumed layered structure might obscure or distort sub-horizontal or vertical structures [73]. Finally, the 3D effect of the fired brick debris and other near surface anthropogenic features can cause erroneous 1D resistivity model. Thus, a 2D formulation is needed to map lateral heterogeneities within the surface archaeological layer.

The inversion results of the long ERT profiles (Figure 7) are visualized and presented as shaded relief georeferenced sections using the Oasis Montaj Program ver. 8.3 [72].

The DD and WB models (Figure 7A and B respectively) yielded comparable results, both being able to image the interface between the upper resistive zone ($>7 \Omega \cdot \text{m}$) and the underlying conductive layer ($<0.5 \Omega \cdot \text{m}$), marked by white dotted lines in (Figure 7A,B). Once again, the surface layer extended to approximately 3 m and was consistent with that derived from excavations. Toward the southern lowland, an approximately 40-m offset distance from the start of the profile, archaeological ruins were inconsiderable. The DD inversion model (Figure 7A) depicts distinct features that could be archaeological structures at shallow depths. However, the WB model (Figure 7B) smeared out the lateral discontinuities. This archaeological layer can be interpreted as a settlement constructed from dissected fired brick walls dated back to an Islamic Era (Figure 7C), considering the archaeological evidence and excavations executed by MATD in 2018 [74]. Conversely, the geoelectrical model obtained by the inversion of the WB dataset (Figure 7B) clearly identifies a high-resistivity zone at a deeper depth (from 10 to 15 m) more accurately than the DD survey (Figure 7A). Since the DD array is more susceptible to off-axis structures (the pitfall in the 2D resistivity survey and inversion due to the lateral 3D effect) and the lower parts of its inverted models suffered the most distortion [75], the deeper part of WB model (Figure 7B) could be interpreted as Gezira sand, which was considered important results and of great interest to the group of archaeology in charge of this site. Since they discovered the western segment of an enclosure (mud-brick wall of Greco-Roman date) nearly 4 m high and 7 m deep (Figure 7D) that protects a probable temple (more than 2000 years ago), the archaeologists who work at Tell Dibgou failed to reach the sand layer on which the temple ruins rests. In light of these collaborative data, the archaeologists should intensify their work in the forthcoming excavation seasons at the heart of the Tell by establishing pits 10 m deep to discover the remains of the Pharaonic Temple.

5.2. Area Around Spot B

Figure 8A shows the correct 3D position of the rectangular area surveyed around Spot B. A visual inspection of the residual magnetic field intensity map (Figure 8B) reveals prominent mutually elongated positive and negative anomalies aligned in NE–SW directions that follow the short side of the surveyed grid. The linear and narrow positive anomalies suggest the presence of fired bricks of stone walls. Figure 8C exhibits a vertical magnetic gradient map. This map appears to have the fewest artifacts and has been interpreted. The magnetic results were characterized by some remarkably continuous linear anomalies that are probably archaeological features. Two perpendicular sets are evident on the vertical-gradient magnetic map. The majority of anomalies are aligned in the NE–SW direction and primarily at the lower central part. Negative elliptical anomalies completely or mostly bounded by linear anomalies can be recognized. The linear anomalies can be attributed to fired brick walls dated back to ancient Islamic settlers. In contrast, the circular negative magnetic anomalies can be interpreted as rooms filled with natural clay sediments. The vertical-gradient anomalies indicate a complex settlement including two or three structures, in which a uniform pattern of walls and rooms (or courtyards) is evident. The tilt angle derivative (TAD) of the vertical magnetic gradient was calculated [76] to outline the edges of the archaeological feature more accurately. The amplitude of the tilt angle has a discrete range (between $-\pi/2$ and $\pi/2$), which can be categorized into positive values located inward from the edge toward the center of the source, zero at or near the edges, and negative values outside the source (Figure 8D). This approach acts well for discriminating the shallow and intermediate sources. Conversely, the sources located far below the surface are blurry [77–79]. The borders of the most interesting anomalies are recognized and highlighted with the zero-radian contour line of the TAD (solid black lines in Figure 8D). Fortunately, the area surveyed was fully uncovered during a campaign in 2018. The physical excavation revealed the main walls, rooms, and corridors of a foundation known from the Islamic Period (the dotted red lines in Figure 8E), which was clearly consistent with the geometry of the geophysical anomalies (Figure 8C, D). The average width of the wall is 75 cm. In some parts of the area, fired brick stones are distributed

irregularly because of human actions, as stones from uninhibited Islamic buildings were reused by the local population to build new constructions in other places. The main wall and internal structures are surrounded and covered by mostly clayey soil.

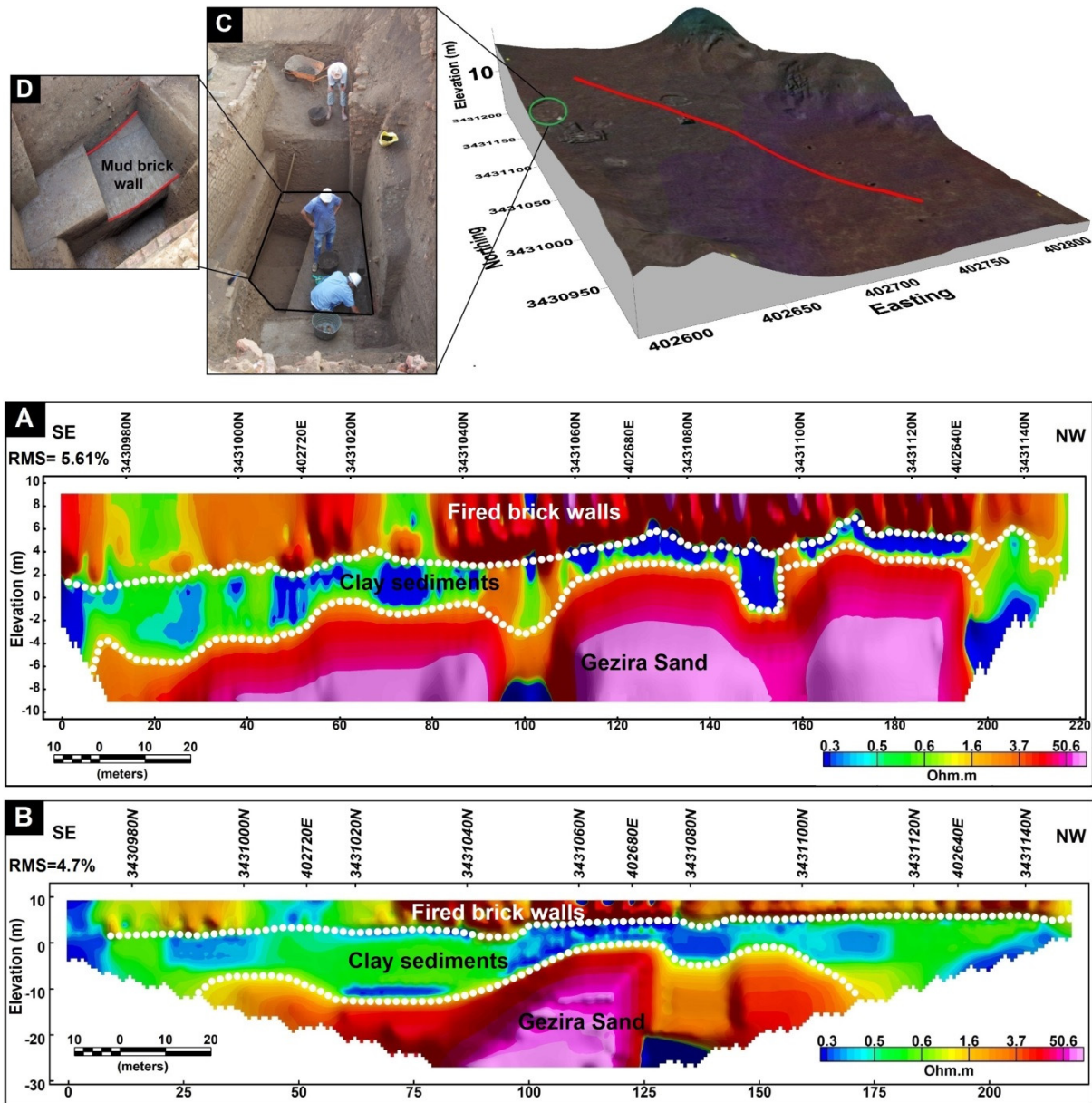


Figure 7. Results of 2D ERT: (A,B) DD and WB inversion models, respectively; and (C,D) photos of excavation during the MATD campaign in September 2019.

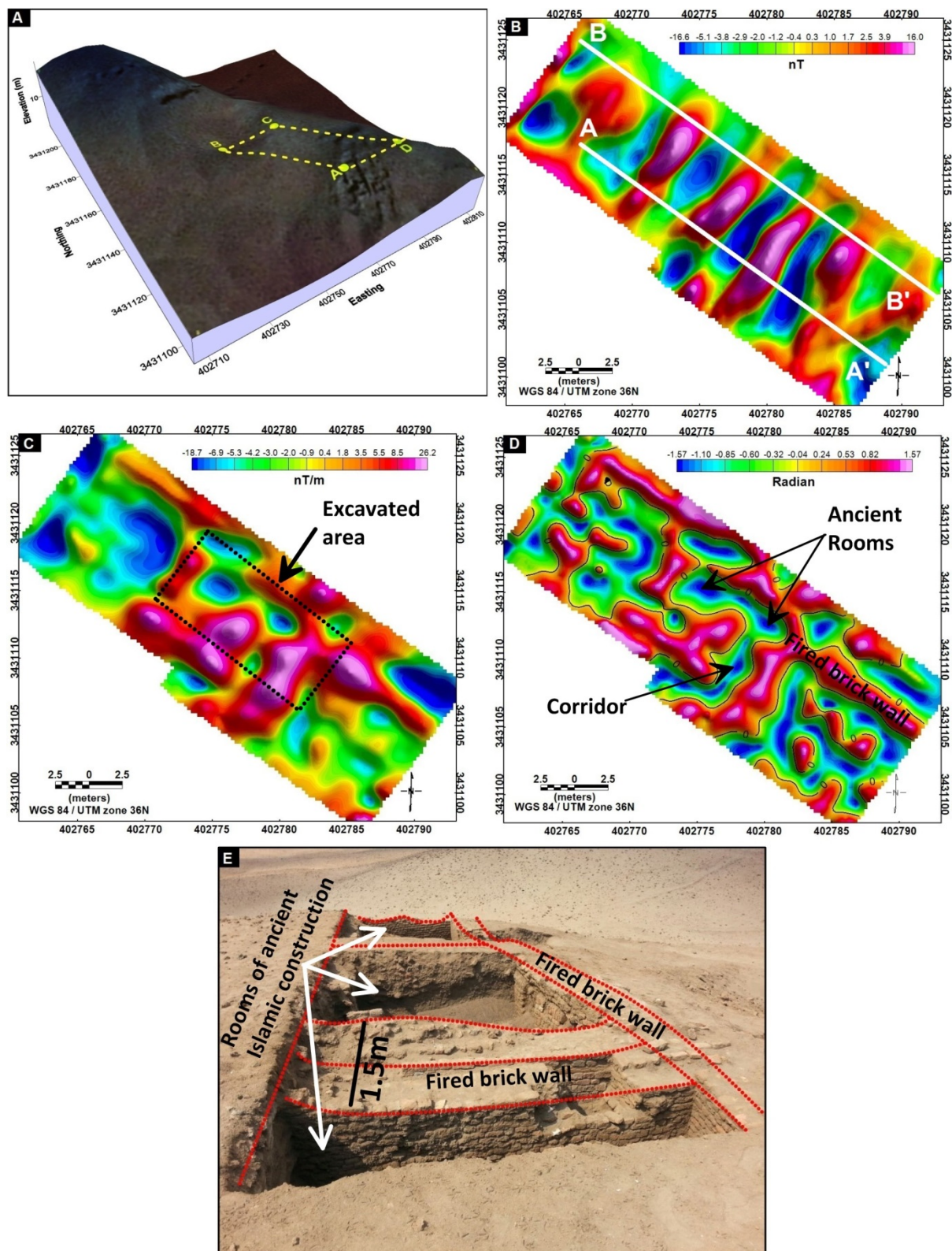


Figure 8. Magnetic results of the area around Spot B: (A) 3D geometry of the actual location of the surveyed area; (B) Butterworth filtered (Ft) map; (C) vertical magnetic gradient using sensors spaced 1.2 m apart; (D) tilt angle derivative of the vertical magnetic gradient; and (E) photo of excavation; dotted lines represent the boundaries of fired brick walls.

Figure 9A exhibits the 3D view of the real positioning of the two ERT profiles employed (DD 1 and DD 2). The true resistivity distributions along inverted ERT sections were

displayed and plotted in a 3D cube with axes of global coordinates (Figure 9B) to facilitate the overlaying between the excavation and the ERT results. The interpretation of these profiles was relatively straightforward in terms of revealing the archaeological units. Along the ERT profiles, the electrical resistivities are limited (from $1 \Omega\cdot\text{m}$ to approximately $20 \Omega\cdot\text{m}$), attributed to soils highly affected by salinization. The inverted profiles specify sharp vertical and horizontal boundaries between archaeological and natural deposits (marked by black dotted lines in Figure 9B). According to resistivity variations in the upper zone and considering the systematic excavation, it is possible to interpret the high-resistivity anomalies ($>7 \Omega\cdot\text{m}$) as walls from an Islamic settlement constructed from fired bricks. It is worth mentioning that combining resistivity data with different electrode spacing (1 and 2 m) increased the resolution at shallower depths. The wall width determined from the ERT image was consistent with the true value (75 cm) (Figure 9C), where the high resolution was obtained by overlapping data levels (combining measurements with different electrode spacing (a) and depth levels (n)). However, slag debris and dense scattered fired bricks from collapsed structures arbitrarily make the interpretation of ERT slightly more difficult, especially in separating adjacent walls. Both the ERT and magnetic results were conformable; however, the superiority of the latter comes from the susceptibility contrast between the fired brick stones and surrounding clayey sediments, which is greater than the resistivity contrast between anthropogenic and natural deposits.

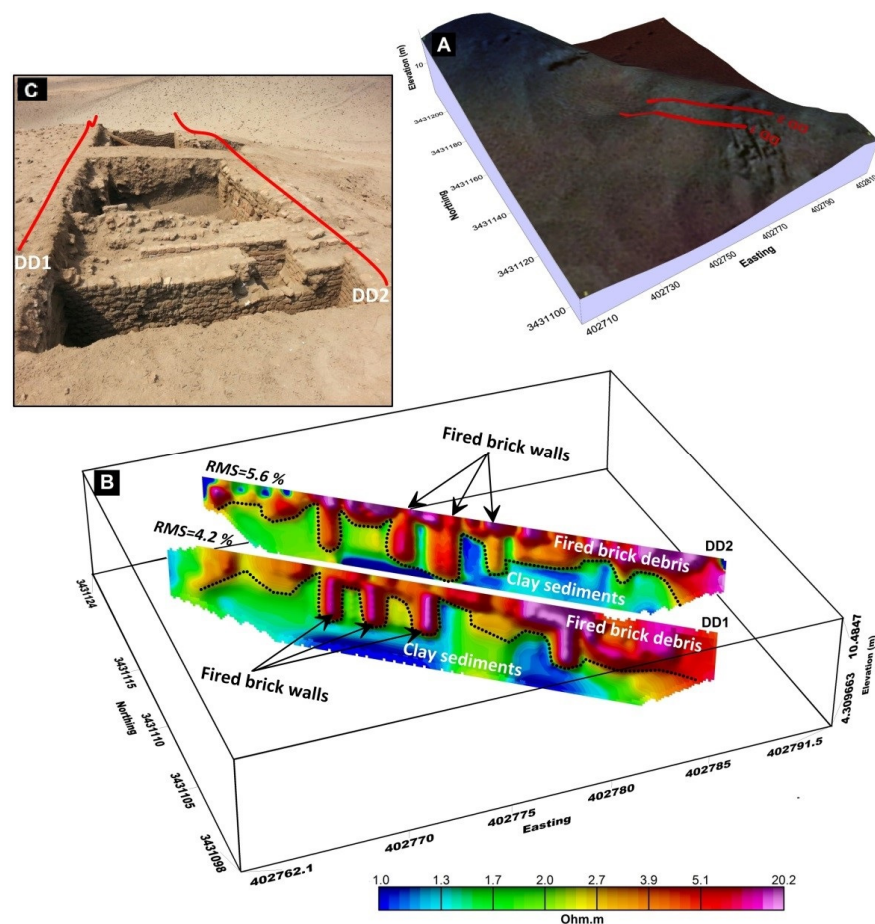


Figure 9. Results of 2D ERT at the area around Spot B: (A) 3D geometry of the actual location of the 2D ERT profiles, DD 1 and DD 2; (B) pseudo-3D inverted models; and (C) photo of an unearthed fired brick wall.

As the archaeological targets have restricted lengths rather than infinite extent, 2.5-dimensional (2.5D) magnetic modeling was conducted using GM-SYS modeling software, version 8.3 [72]. The profiles AA' and BB' run in the SE–NW direction with a distance

of 27 m along the Butterworth filtered map (Figure 8B). This direction parallels the trend direction of many linear features but shows variations due to linear features trending NE–SW. In this case, the modeling was constrained by the results of 2D resistivity imaging to reduce all possibilities and solutions to only a few appropriate and plausible models. The magnetic models were superimposed on the 2D ERT inverted section.

Both profiles were modeled similarly by constructing blocks representing the fired brick walls with an average magnetic susceptibility of about 0.0027 in cgs units. In many cases, these blocks are placed in the center or edge of a vertical resistive anomaly (Figure 10). The width of each wall is 0.75 m and extends to a maximum depth of approximately 3 m. The best fit between the measured and calculated magnetic anomalies was obtained by extending the modeled walls by 3 m on both sides (NNE–SSW) perpendicular to the magnetic profiles. Subsequently, the effect of the walls' strike length was taken into consideration during the modeling process. Natural clay sediments represented the lower part of the model with very low magnetic susceptibility (0.0005 cgs) and very low resistivity. Along the profiles, the topmost part was exemplified by slag debris and scattered fired bricks in decreasing amounts in the northwest direction. The RMS errors of about 0.149 and 0.157 for profiles AA' and BB', respectively, indicate a satisfactory fit between the observed and calculated magnetic anomalies. The position (location and depth) of the interpreted walls correlated with subsequent archaeological excavations in the area during August 2018.

5.3. Area Around Spot C

The results of the magnetic and quasi-3D resistivity imaging surveys at the area around Spot C are presented here. The joint application offers the opportunity to discuss the interrelation between the nearby fully excavated worship place (probably a church) and the area surveyed. The 3D geometry of the area's actual location covered by the magnetic survey is given in Figure 11A. The local magnetic anomalies of shallow archaeological origin were isolated from the regional field of deeper sources using high-pass Butterworth filtering with a cutoff wavelength of 1.5 m (Figure 11B). The spatial contrast in the amplitudes of magnetic anomalies could imply sources located at different depths or might be due to different types of buried remains. A high-magnitude prominent anomaly was located at the southern part of the surveyed site and encircled by two anomalies of negative polarity. In addition, the first vertical derivative was calculated (Figure 11C) to better delineate the lateral boundaries of archaeological features of different susceptibilities. The high-pass filtered magnetic and first vertical derivative maps (Figure 11B,C, respectively) have comparable results, notably similar anomalies in terms of patterns and locations. However, the latter produced much more resolved boundaries of the magnetic sources. The 3D Euler deconvolution technique was applied to the magnetic data to outline the possible source locations and estimate the depths of the source bodies. A range of structure indices (SIs) was examined to choose the best one based on solutions clustering. The resulting Euler solutions, using an SI of 0 and a window size of 2.5 m × 2.5 m, are jointly represented in the vertical derivative map (Figure 11D), where the clusters of located Euler solutions follow the anomaly patterns much more closely. In view of the solution map, some rectilinearity was produced above the edges of the archaeological targets. The estimated depths of the magnetic sources of archaeological origin ranged from approximately 0.2 to 3.54 m, which are logical depending on the general information provided from previous excavations all over the site. As is well known, the vertical gradient is typically preferred over the total field in archaeological prospecting; however, at this site, the presence of dense scattering of magnetized slag debris (broken fired bricks) affected greatly the lower sensor (0.6 m) measurements and thus produced deteriorated and unreadable gradient map (Figure 11E).

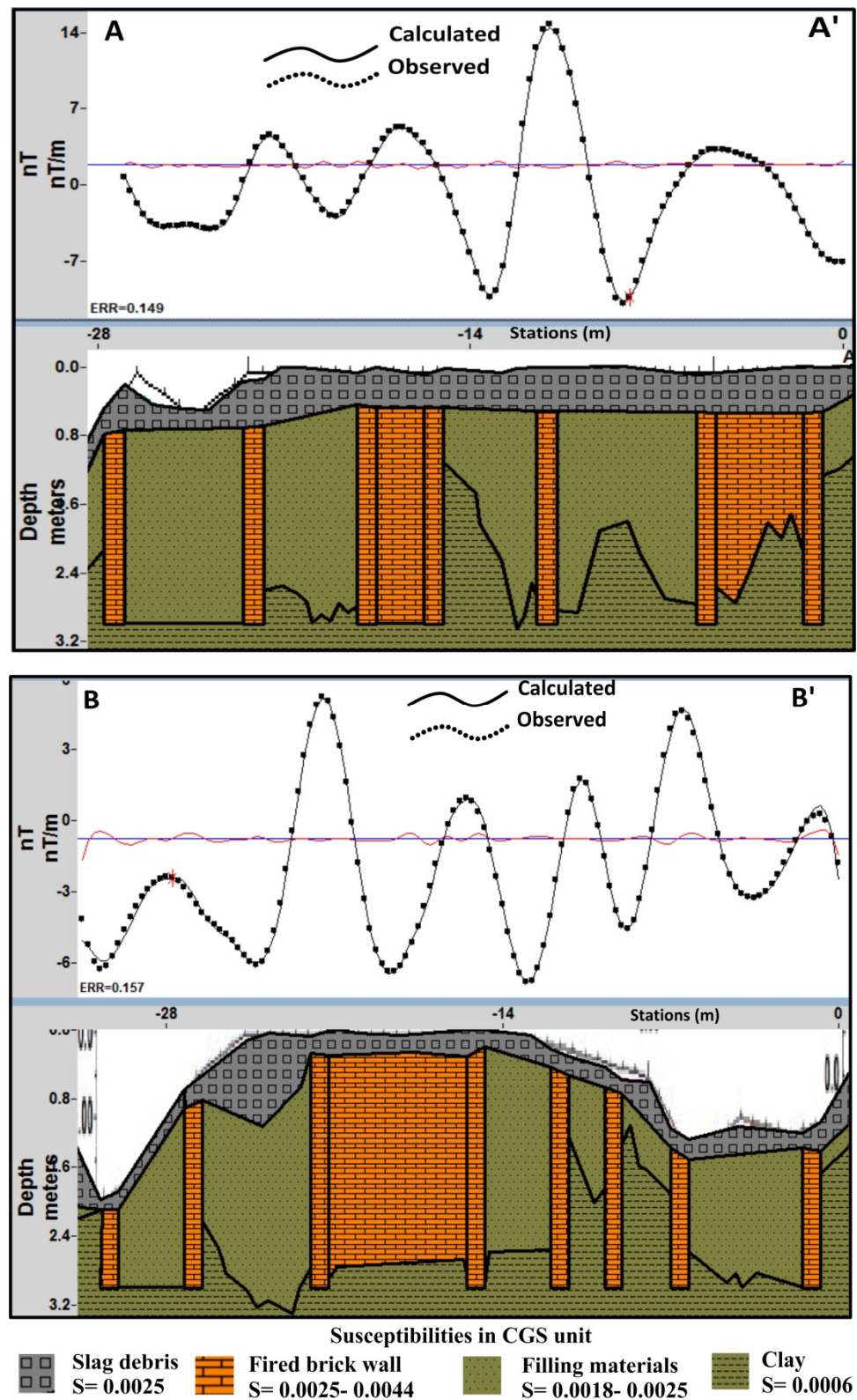


Figure 10. The 2.5-dimensional magnetic modeling along profiles: (A) AA'; and (B) BB'.

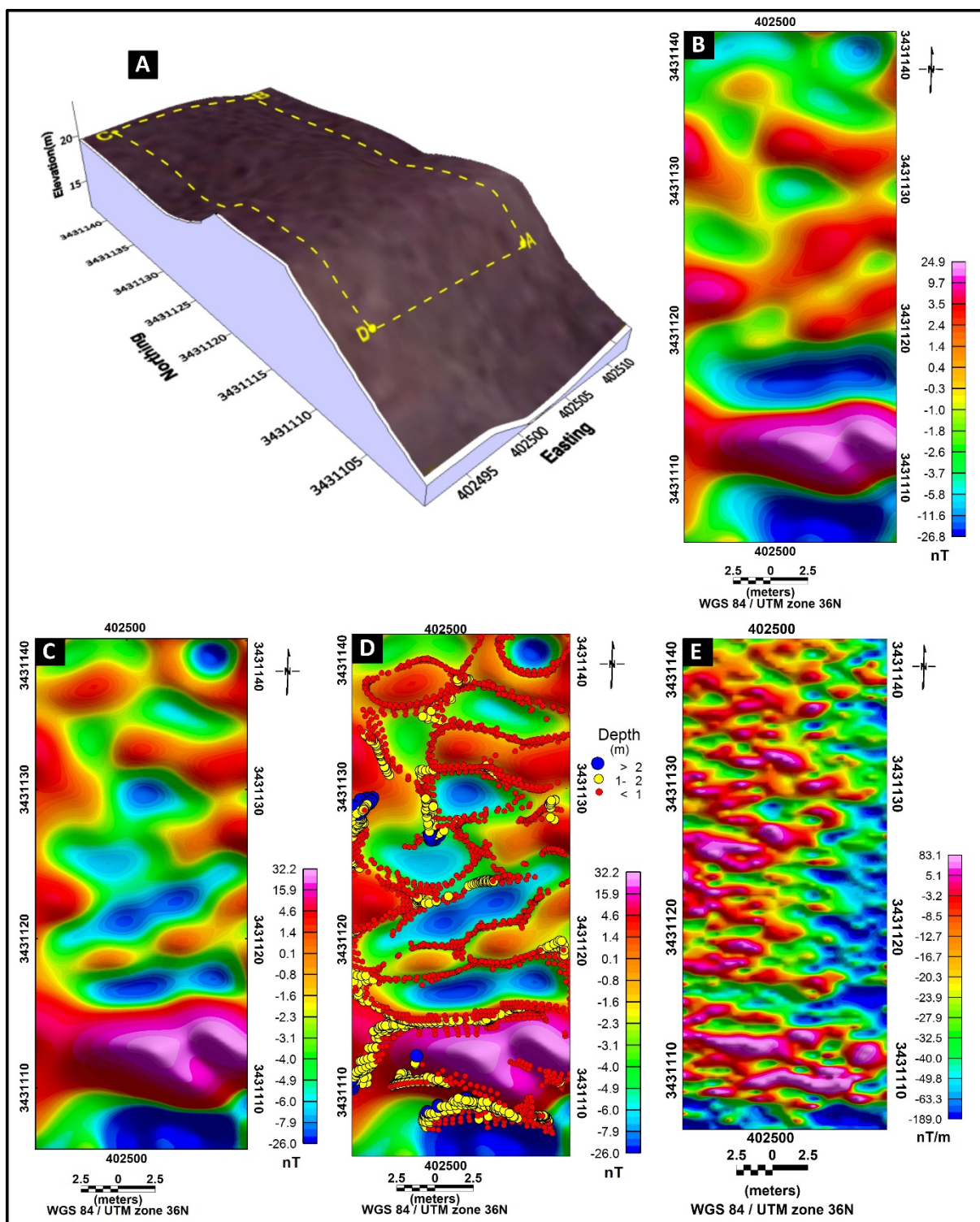


Figure 11. Magnetic results at the area around Spot C: (A) 3D geometry of the actual location of the area covered by the magnetic survey; (B) Butterworth filtered map; (C) first vertical derivative map; (D) 3D Euler deconvolution solutions superimposed onto the first vertical derivative map; and (E) vertical gradient using sensors spaced 0.6 m apart.

Figure 12A displays the georeferenced location of the executed 2D ERT transects which cross the anomalous magnetic zones. In all 2D inversion runs, using different settings, the models show similar features. Inverted models of the resistivity sections display a depth range of approximately 5 m, with RMS errors ranging between 2.5% and 6.8%.

The five inverted ERT sections were gathered into a 3D block view (Figure 12B). A wide domain of resistivity values is shown by all inversion models. Sharp resistivity contrasts are evident in all images that exhibit similar features in terms of geometry, orientation, and dimension, signifying the presence of buried remains, thus outlining possible man-made structures. Of particular interest is the anomaly displaying high resistivity ($>1500 \Omega\cdot\text{m}$), which cuts through the low relief of the whole inverted 2D ERT sections and is visible from the surface to the bottom of the inverted sections (Figure 12B). It is clearly distinguished from the adjacent moderate- to low-resistivity patterns. The inversion of 3D-quasi-parallel profiles was implemented to enhance the interpretation of the geoelectrical resistivity survey. The inverted 3D resistivity model was obtained after 12 iterations with an RMS error of 6.74% and displayed as a working resistivity cube (WRC), rendered iso-resistivity images, and depth slices (Figure 12C–E, respectively). The WRC (Figure 12C) detected an interesting circular high-resistivity anomaly extending roughly southward and emerging above the rest of the geoelectric anomalies. Figure 12D displays the 3D contouring of iso-resistivity surfaces defined by threshold values ranging from 1500 to 5000 $\Omega\cdot\text{m}$ to image the morphology of the already described high-resistivity anomaly. This type of visualization ensured the location of potential buried archaeological structures with higher resistivity values than the surrounding soil and slag. In addition, the quasi-3D inversion outcome was visualized across seven resistivity-depth slices of a logarithmic rainbow scale (Figure 12E). The subsurface resistivity distribution indicates a distinct anomaly, almost forming a rectangle of high resistivities (red colors), which was revealed in the southern part close to materials with relatively moderate to low resistivities (blue and green colors). It encloses an area of approximately $15 \text{ m} \times 12 \text{ m}$ and can be traced from the first to the bottom depth slices. To the north, down to a depth of approximately 1 m, random isolated arbitrarily shaped anomalies could correspond to scattered fired brick stones. At deeper depths (greater than 1 m), the amount of fired stone debris is reduced, and the dominant materials are presumably represented by clayey and moist filling materials. Unfortunately, to date, no systematic archaeological excavation has been conducted at this site. Thus, the 3D reconstructed source images cannot be compared with historical and archaeological knowledge. However, the two reasonable archaeological models of the inferred anomaly, based on nearby excavations to the southeast of the surveyed area, are a water cistern and an underground room or a vault used as a chapel or burial place (crypt). During the last MATD campaign in 2019 [49], large water cisterns, reinforced with buttresses, were found installed inside the excavated worship place and certainly supplied the main mosque of the city during the reign of Ibn Tulun (Figure 12F).

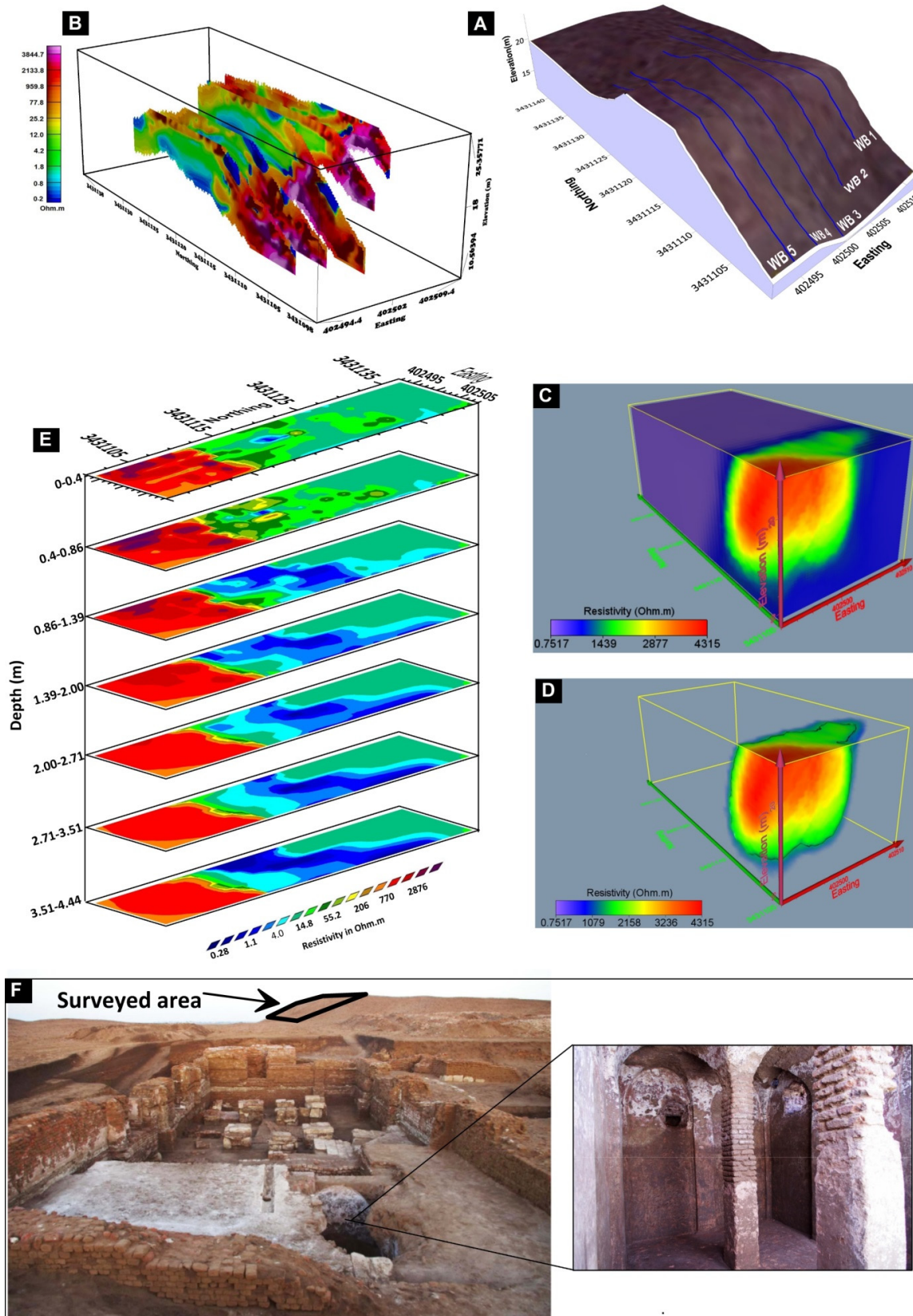


Figure 12. Results of 3D-quasi-ERT at the area around Spot C: (A) 3D geometry of the actual location of the five measured parallel profiles; (B) pseudo-3D inverted models along five parallel profiles; (C) working resistivity cube of the 3D inversion results; (D) 3D visualization of iso-resistivity surfaces; (E) horizontal resistivity-depth slices from 0 to 4.4 m; and (F) general view of the church unearthed in the heart of the medieval city of Dibgou by the MATD campaign in September 2019.

The combined representation of Euler deconvolution solutions and resistivity-depth slices is given in Figure 13. It can be noticed that the source-edge locations obtained using the Euler deconvolution techniques approximately surrounded the high-resistivity zones.

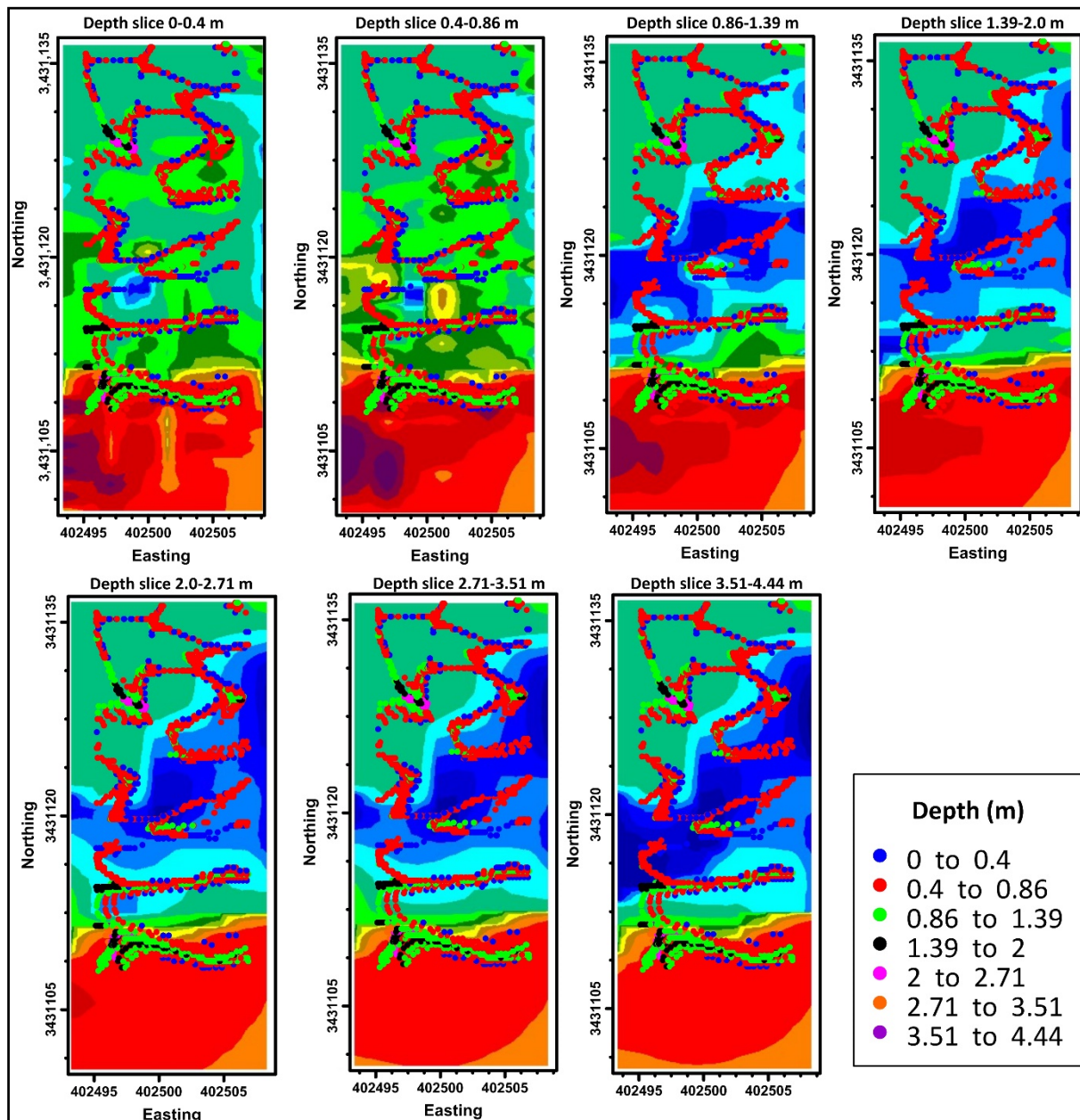


Figure 13. Combined representations of the Euler deconvolution solutions superimposed onto resistivity-depth slices.

5.4. Area Around Spot D

At this site, the magnetic survey covered an area of about 160 m² (Figure 14A). The RTP magnetic map around Spot D is given in Figure 14B and displays a circular, broad positive anomaly in the middle, indicating a 3D magnetic body. The radial average power spectrum was used to isolate the shallow and deep components, and the transition was interpreted to be at a wavenumber of 180 radians/m (equivalent to a cutoff wavelength of 5.6 m). The high-pass filtered RTP magnetic map (Figure 14C) has removed the long wavelengths associated with deeper magnetic bodies. Hence, this image highlights the anomalies associated with shallower magnetic bodies. Although the anomalies are small (−13 to 6 nT), there is a great likelihood that the magnetic anomaly indicates an archaeological

architecture. The shape and size of this magnetic feature are similar to those of a nearby water tank (approximately 100 m to the north of the investigated area) constructed using fired bricks, dated to the Byzantine Era (Figure 14D).

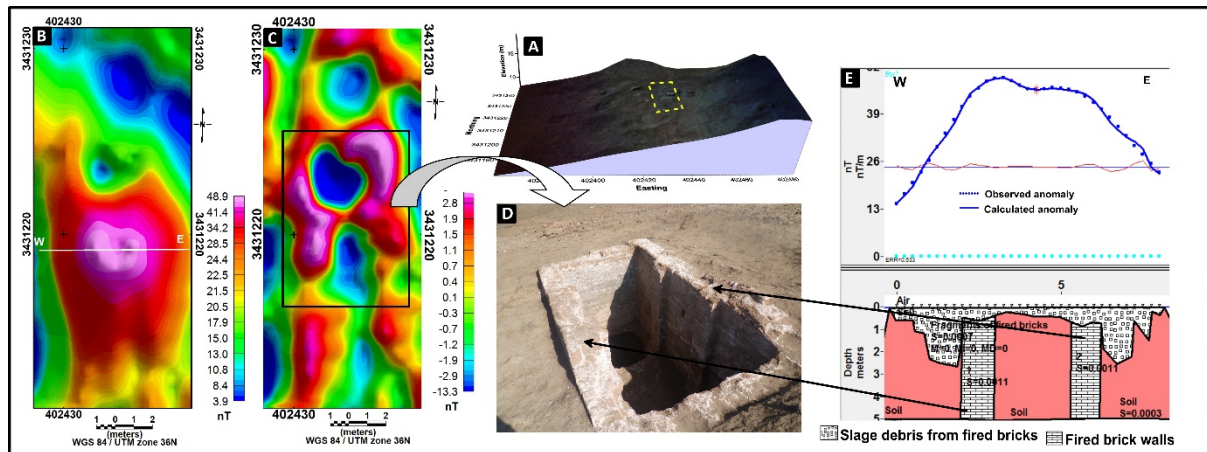


Figure 14. Magnetic results at the area around Spot D: (A) 3D geometry of the actual location of the area covered by the magnetic survey; (B) RTP magnetic map; the solid white line indicates the magnetic profile to be modeled; (C) high-pass filtered map using a cutoff wavenumber of 180 Radians/m; (D) a nearby excavated water tank; and (E) 2.5D modeling.

This hypothesis can be strengthened by modeling a water tank along the 8-m profile shown in white in Figure 14A. Once again, a 2.5D magnetic modeling was constructed using GM-SYS software version 8.3 [72]. A good fit between the observed and calculated responses with an RMS error of 0.633 nT was achieved. The best parameters that yielded a reasonable empirical response consistent with the conceptual archaeological model are shown in Figure 14E. In this model, the depth to the top of the water tank walls is about 0.5 m, the width is 0.75 m, and the magnetic susceptibilities are 0.0011, 0.0007, and 0.0003 cgs units for the walls, covering slag debris, and hosting clay sediments, respectively.

6. Conclusions

From the integration of geophysical survey and systematic excavations at Tell Dibgou, four occupation periods (Pharaonic, Byzantine, Greco-Roman, and Islamic Eras) are represented at different depths. The magnetic method effectively identified walls, water tanks, and a crypt or water cistern at shallow depths. This is believed to be because the most dominant archaeological features are made of fired bricks, which have higher magnetic susceptibility than the surrounding clayey soils. Further, the vertical magnetic gradient using sensors 1.2 m apart produced superior results in identifying near-surface walls constructed from fired brick stones in the eastern part of the Tell. Unexpectedly, the same approach, using a closer sensor distance (0.6 m) at the northern site, produced deteriorated and unreadable images because the bottom sensor height (0.6 m) is close enough to the surface noise represented by fired brick debris. Butterworth filtering, the tilt angle, and first vertical derivatives provided simple and clean images that were easy to interpret. All techniques tended to enhance the mapping of subtle magnetic anomalies and maximize the characterization of the geometrical contrasts of anomalous sources.

On another note, the resistivity method was better in identifying archaeological ruins at different depths with different resolutions. At the heart of the Tell, both 1D resistivity sounding and 2D ERT surveys revealed the presence of a relatively resistive sandy layer (Gezira sand) with an irregular upper surface approximately 10 m below the ground surface. This layer is of great interest to the group of archaeologists working at the Tell. Furthermore, the quasi-3D ERT inversion scheme worked well in the northern part of the Tell. The inverted dataset was displayed in different 3D views (WRC, rendered, and

iso-resistivity maps and depth slices). Each view has its advantages in delineating the anomaly of archaeological origin, especially the prominent southern one.

Grouping together the geophysical datasets with different attributes (ED solutions and resistivity-depth slices) and viewing the maps simultaneously simplify the correlation of geophysical data—one to one—necessary to validate the interpretation. In this context, the 3D Euler deconvolution solutions and resistivity-depth slices showed partial agreement regarding locations and depths. In addition, the 2.5D magnetic modeling, constrained by 2D ERT imaging, allowed detailed effective identifications of buried walls in a noisy environment. Moreover, a crucial aspect in archaeogeophysics is the georeferencing of all geophysical data because the results are then linked to subsequent excavations.

All archaeological findings based on geophysics fit well with those of previous systematic excavations conducted by the MATD. Additionally, the information provided in this investigation can be used to plan future archaeological excavations, notably at the heart and northern parts of the Tell. The applied multi-geophysical methodologies approach and data analysis has provided a significant improvement in the interpretation and visualization facilities in terms of buried walls for the future employment of geophysical and archaeological datasets at complex and highly terraneous sites elsewhere. Therefore, DC resistivity (DCR) can contribute to identify subsurface zones to fill the information gap of archaeological stratigraphy, while resistivity imaging (2D/3D) created from resistivity datasets was verified to be a useful tool in demonstration of the archaeological structures in clay background. In contrast, the magnetic method is best for identifying magnetic (fired brick) walls. In the latter case, slag and loose bricks might be a source of noise.

Author Contributions: This work was made possible by significant contributions from all authors. A.I., K.S.G., and S.A.S., Conceptualization, Methodology (ERT and magnetic), Formal analysis (Geophysical data modeling), Investigation (Magnetic and ERT). A.I., and S.A.S., Data Curation (geophysical metadata). A.I. and K.S.G., Original Draft, Writing—Review & editing the final MS, Visualization and presentation of geophysical data datasets. K.A., N.A.-O., and E.I., Corresponding, Review & editing the final MS. All authors contributed critically to the drafts and gave final approval for publication. All authors have read and agreed to the published version of the manuscript.

Funding: The Deanship of Scientific Research at King Saud University: research group No. RGP -1436-011.

Institutional Review Board Statement: Not applicable.

Informed Consent Statement: Not applicable.

Data Availability Statement: The data that support the findings of this study are available from the corresponding author upon reasonable request.

Acknowledgments: The authors extend their appreciation to the Deanship of Scientific Research at King Saud University for funding this work through research group No. RGP -1436-011.

Conflicts of Interest: The authors declare that they have no known competing financial interests or personal relationships that could have appeared to influence the work reported in this paper.

Appreciation: The authors extend their great appreciation to both of Metwally Salama, the Director of Antiquities of Eastern Nile Delta Sector, and Philippe Brissaud, the director of the French Mission of Archaeology at the site of interest (MATD), for their valuable information and guidance through the field survey.

References

1. Campana, S.; Piro, S. *Seeing the Unseen. Geophysics and Landscape Archaeology*; Taylor & Francis: London, UK, 2009; p. 376.
2. Belvedere, O. Archaeological Survey in Italy between Ancient Topography and Landscape Archaeology. In *Göttinger Studien zur Mediterranen Archäologie Bd. 8*; Verlag Marie Leidorf GmbH: Rahden, Germany, 2017; ISBN 978-3-86757-507-2.
3. Trinks, I.; Neubauer, W.; Doneus, M. *Prospecting Archaeological Landscapes*; Springer: Berlin/Heidelberg, Germany, 2012; pp. 21–29.
4. Trinks, I.; Neubauer, W.; Hinterleitner, A. First high-resolution GPR and magnetic archaeological prospection at the Viking age settlement of Birka in Sweden. *Archaeol. Prospect.* **2014**, *21*, 185–199. [[CrossRef](#)]

5. Gustavsen, L.; Stamnes, A.A.; Fretheim, S.E.; Gjerpe, L.E.; Nau, E. The Effectiveness of Large-Scale, High-Resolution Ground-Penetrating Radar Surveys and Trial Trenching for Archaeological Site Evaluations—A Comparative Study from Two Sites in Norway. *Remote Sens.* **2020**, *12*, 1408. [[CrossRef](#)]
6. Cardarelli, E.; Di Filippo, G. Integrated geophysical methods for the characterisation of an archaeological site (Massenzio Basilica—Roman forum, Rome, Italy). *J. Appl. Geophys.* **2009**, *68*, 508–521. [[CrossRef](#)]
7. Hegyi, A.; Diaconescu, D.; Urdea, P.; Sarris, A.; Pisz, M.; Onaca, A. Using Geophysics to Characterize a Prehistoric Burial Mound in Romania. *Remote Sens.* **2021**, *13*, 842. [[CrossRef](#)]
8. Drahor, M.G.; Berge, M.A.; Öztürk, C. Integrated geophysical surveys for the subsurface mapping of buried structures under and surrounding of the Agios Voukolos Church in İzmir, Turkey. *J. Archaeol. Sci.* **2011**, *38*, 2231–2242. [[CrossRef](#)]
9. Küçükdemirci, M.; Piro, S.; Ozer, E.; Baydemir, N.; Zamuner, D. An integrated Geophysical Survey at Aizanoi Archaeological site (Turkey). In Proceedings of the 11th International Conference on Archaeological Prospection ICAP2015, Warsaw, Poland, 15–19 September 2015; *Archaeologia Polona*. pp. 477–479, ISSN: 0066-5924.
10. Küçükdemirci, M.; Özer, E.; Piro, S.; Baydemir, N.; Zamuner, D. An application of integration approaches for archaeo-geophysical data: Case study from Aizanoi. *Archaeol. Prospect.* **2018**, *25*, 33–44. [[CrossRef](#)]
11. Abu Zeid, N.; Corradini, E.; Bignardi, S.; Morandi, N.; Nizzo, V. The passive seismic technique “HVSR” as a reconnaissance tool for mapping paleo-soils: The case of the Pilastris archaeological site, Northern Italy. *Archaeol. Prospect.* **2017**, *24*, 245–258. [[CrossRef](#)]
12. Deiana, R.; Bonetto, J.; Mazzariol, A. Integrated Electrical Resistivity Tomography and Ground Penetrating Radar Measurements Applied to Tomb Detection. *Surv. Geophys.* **2018**, *39*, 1081–1105. [[CrossRef](#)]
13. Arka, I.; Balkaya, Ç.; Pülz, A.; Alanyali, H.S.; Kaya, M.A. Integrated geophysical investigations to reconstruct the archaeological features in the episcopal district of side (Antalya, southern Turkey). *J. Appl. Geophys.* **2019**, *163*, 22–30. [[CrossRef](#)]
14. Abu Zeid, N.M.; Bignardi, S.; Russo, P.; Peresani, M. Deep in a Paleolithic archive: Integrated geophysical investigations and laser-scanner reconstruction at Fumane Cave, Italy. *J. Archaeol. Sci. Rep.* **2019**, *27*, 1–10. [[CrossRef](#)]
15. Gaber, A.; Gemail, K.S.; Kamel, A.; Atia, H.M.; Ibrahim, A. Integration of 2D/3D ground penetrating radar and electrical resistivity tomography surveys as enhanced imaging of archaeological ruins: A case study in San El-Hager (Tanis) site, northeastern Nile Delta, Egypt. *Archaeol. Prospect.* **2021**. [[CrossRef](#)]
16. Schmidt, A. Electrical and magnetic methods in archaeological prospection. In *Seeing the Unseen. Geophysics and Landscape Archaeology*; Campana, S., Piro, S., Eds.; Taylor and Francis Group: London, UK, 2009; pp. 67–81.
17. Salvatore, P.; Enrico, P.; Daniela, Z.; Melda, K. Multimethodological approach to investigate urban and suburban archaeological sites. In *Innovation in Near-Surface Geophysics*; Elsevier BV: Amsterdam, The Netherlands, 2019; pp. 461–504. [[CrossRef](#)]
18. Tsokas, G.N.; Hansen, R.O. On the use of complex attributes and the inferred source parameter estimates in the exploration of archaeological sites. *Archaeol. Prospect.* **2000**, *7*, 17–30. [[CrossRef](#)]
19. Dabas, M.; Anest, A.; Thiesson, J.; Tabbagh, A. Slingram EMI Devices for Characterizing Resistive Features Using Apparent Conductivity Measurements: Check of the DualEM-421S Instrument and Field Tests. *Archaeol. Prospect.* **2016**, *23*, 165–180. [[CrossRef](#)]
20. Gaffney, C.; Gater, J.A.; Ovenden, S.M. *The Use of Geophysical Techniques in Archaeological Evaluations*; IFA Technical Paper 6; Reading Institute of Field Archaeologists, University of Reading: Reading, UK, 2002; ISBN 0 948393 16 3.
21. Chianese, D.V.; Lapenna, S.; Di Salvia, S.; Perrone, A.; Rizzo, E. Joint geophysical measurements to investigate the Rossano of Vaglio archaeological site (Basilicata region, southern Italy). *J. Archaeol. Sci.* **2010**, *37*, 2237–2244. [[CrossRef](#)]
22. Danielsen, B.E.; Dahlin, T. Comparison of geoelectrical imaging and tunnel documentation. *Eng. Geol.* **2009**, *107*, 118–129. [[CrossRef](#)]
23. Rønning, J.S.; Ganerød, G.V.; Dalsegg, E.; Reiser, F. Resistivity mapping as a tool for identification and characterisation of weakness zones in crystalline bedrock: Definition and testing of an interpretational model. *Bull. Eng. Geol. Environ.* **2014**, *73*, 1225–1244. [[CrossRef](#)]
24. Eppelbaum, L.V. Study of magnetic anomalies over archaeological targets in urban conditions. *Phys. Chem. Earth* **2011**, *36*, 1318–1330. [[CrossRef](#)]
25. Lapenna, V. Resilient and sustainable cities of tomorrow: The role of applied geophysics. *Boll. Geofis. Teor. Appl.* **2017**, *58*, 237–251. [[CrossRef](#)]
26. Smriglio, F.; Papale, E.; Verga, F.; Piro, S. Noninvasive geophysical integrated survey at Madonna del Giglio (Sabine necropolis, Magliano Sabina, Latium, Central Italy). *Archaeol. Anthr. Sci.* **2020**, *12*, 1–12. [[CrossRef](#)]
27. Krauss, L.; Klasen, N.; Schulte, P.; Lehmkuhl, F. New results concerning the pedo- and chronostratigraphy of the loess–palaeosol sequence Attenfeld (Bavaria, Germany) derived from a multi-methodological approach. *J. Quat. Sci.* **2021**. [[CrossRef](#)]
28. Welc, F.; Mieszkowski, R.; Vrkljan, G.L.; Konestra, A. An Attempt to Integration of Different Geophysical Methods (Magnetic, GPR and ERT); A Case Study From the Late Roman Settlement On the Island of Rab in Croatia. *Stud. Quat.* **2017**, *34*, 47–59. [[CrossRef](#)]
29. Florio, G.; Cella, F.; Speranza, L.; Castaldo, R.; Benoit, R.P.; Palermo, R. Multiscale techniques for 3D imaging of magnetic data for archaeo-geophysical investigations in the Middle East: The case of Tell Barri (Syria). *Archaeol. Prospect.* **2019**, *26*, 379–395. [[CrossRef](#)]
30. Li, M.; Zhang, Z.; Yang, J.; Xie, S. Integrated geophysical study in the cemetery of Marquis of Haihun. *Archaeol. Prospect.* **2021**, *1*, 13. [[CrossRef](#)]
31. Clark, A. *Seeing Beneath the Soil: Prospecting Methods in Archaeology*, 2nd ed.; B.T. Batsford: London, UK, 1996.

32. Cammarano, F.; Di Fiore, B.; Patella, D.; Mauriello, P. Examples of application of electrical tomographies and radar profiling to cultural heritage. *Ann. Geophys.* **2000**, *43*, 309–324.
33. Campana, S.; Dabas, M.; Marasco, L.; Piro, S.; Zamuner, D. Integration of remote sensing, geophysical surveys and archaeological excavation for the study of a medieval mound (Tuscany-Italy). *Archaeol. Prospect.* **2009**, *16*, 167–176. [[CrossRef](#)]
34. El-Qady, G.; Metwaly, M.; Drahor, M.G. Geophysical Techniques Applied in Archaeology. In *Natural Science in Archaeology*; Springer Science and Business Media LLC: Berlin/Heidelberg, Germany, 2018; pp. 1–25. [[CrossRef](#)]
35. Pro, C.; Caldeira, B.; De Tena, M.T.; Charro, C.; Oliveira, R.J.; Borges, J.F.; Mayoral, V. Exploring the Consistency of Data Collected in Archaeological Geophysics: A Case Study from the Iron Age Hillfort of Villasviejas del Tamuja (Extremadura, Spain). *Remote Sens.* **2020**, *12*, 1989. [[CrossRef](#)]
36. Edemsky, D.; Popov, A.; Prokopovich, I. Geophysical survey of Tunnug mound periphery, Tuva, Russia. *J. Appl. Geophys.* **2021**, *189*, 104326. [[CrossRef](#)]
37. Gaffney, C.F.; Gater, J.A.; Linford, P.; Gaffney, V.L.; White, R. Large-scale systematic fluxgate gradiometry at the roman city of Wroxeter. *Archaeol. Prospect.* **2000**, *7*, 81–99. [[CrossRef](#)]
38. Zhai, G.; Bian, G.; Huang, M. A new method to calculate the vertical derivatives of total field magnetic anomaly. *Acta Geod. Cartogr. Sin.* **2011**, *40*, 671–678.
39. Li, Y.; Oldenburg, D.W. Fast inversion of large-scale magnetic data using wavelet transforms and a logarithmic barrier method. *Geophys. J. Int.* **2003**, *152*, 251–265. [[CrossRef](#)]
40. Von Der Osten-Woldenburg, H.; Chaume, B.; Reinhard, W. New archaeological discoveries through magnetic gradiometry: The early Celtic settlement on Mont Lassois, France. *Geophysics* **2006**, *25*, 46–48. [[CrossRef](#)]
41. Loke, M.; Chambers, J.; Rucker, D.; Kuras, O.; Wilkinson, P. Recent developments in the direct-current geoelectrical imaging method. *J. Appl. Geophys.* **2013**, *95*, 135–156. [[CrossRef](#)]
42. Gmail, K.S. Application of 2D resistivity profiling for mapping and interpretation of geology in a till aquitard near Luck Lake, Southern Saskatchewan, Canada. *Environ. Earth Sci.* **2015**, *73*, 923–935. [[CrossRef](#)]
43. Fischanger, F.; Catanzariti, G.; Comina, C.; Sambuelli, L.; Morelli, G.; Barsuglia, F.; Ellaithy, A.; Porcelli, F. Geophysical anomalies detected by electrical resistivity tomography in the area surrounding Tutankhamun’s tomb. *J. Cult. Herit.* **2019**, *36*, 63–71. [[CrossRef](#)]
44. Abu Salem, H.; Gmail, K.S.; Nosair, A.M. A multidisciplinary approach for delineating wastewater flow paths in shallow groundwater aquifers: A case study in the southeastern part of the Nile Delta, Egypt. *J. Contam. Hydrol.* **2021**, *236*, 103701. [[CrossRef](#)] [[PubMed](#)]
45. Griffiths, D.H.; Barker, R.D. Electrical Imaging in Archaeology. *J. Archaeol. Sci.* **1994**, *21*, 153–158. [[CrossRef](#)]
46. Schmidt, A. Archaeology, magnetic methods. In *Encyclopedia of Geomagnetism and Paleomagnetism*; Encyclopedia of Earth Sciences Series; Gubbins, D., Herrero-Bervera, E., Eds.; Springer: Heidelberg, NY, USA, 2007.
47. Masini, N.; Capozzoli, L.; Romano, G.; Sieczkowska, D.; Sileo, M.; Bastante, J.; Victoria, F.A.; Ziolkowski, M.; Lasaponara, R. Archaeogeophysical-Based Approach for Inca Archaeology: Overview and one operational application. *Surv. Geophys.* **2018**, *39*, 1239–1262. [[CrossRef](#)]
48. Gmail, K.S.; El Alfy, M.; Ghoneim, M.F.; Shishtawy, A.M.; El-Bary, M.A. Comparison of DRASTIC and DC resistivity modeling for assessing aquifer vulnerability in the central Nile Delta, Egypt. *Environ. Earth Sci.* **2017**, *76*, 350. [[CrossRef](#)]
49. Brissaud, A.; Desbordes, C. Activity Report—2019 Campaign, MATD, Mission of Archaeology at Tell Dibgou, No 33, 23P. 2019. Available online: <http://www.telldibgou.fr/index.php/rapports-d-activite/2019> (accessed on 1 March 2020).
50. Said, R. *The Geological Evolution of the River Nile*; Springer: Berlin/Heidelberg, Germany, 1981; p. 151.
51. Wit, H.E.; Stralen, L. *Preliminary Results of the 1987 Palaeo-Geographical Survey*; van der Brink, E.C.M., Ed.; The archaeology of the Nile Delta: Amsterdam, The Netherlands, 1988; pp. 135–139.
52. Bietak, M. *Tell el-Daba II*; OCoLC 776782539; Verlag der Österreichischen Akademie der Wissenschaften: Wien, Austria, 1975.
53. Abu Al Izz, M.S. *Landforms of Egypt*; The American University Press: Lanham, MD, USA, 1977; p. 283.
54. Elwan, A.A.; Harga, M.A.; El Kadi, H.A.; El Demerdash, S. Preliminary studies on the soil of North Sinai Peninsula on aerial photo interpretation. *Egypt. J. Soil Sci.* **1983**, *23*, 37.
55. Reid, A.B. Aeromagnetic survey design. *Geophysics* **1980**, *45*, 973–976. [[CrossRef](#)]
56. Reynolds, J.M. *An introduction to Applied and Environmental Geophysics*, 2nd ed.; Wiley-Blackwell: New York, NY, USA, 2011; ISBN 978-0-471-48535-3.
57. Loke, M.H. Rapid 2-D Resistivity and IP Inversion Using the Least-Squares Method. 2018. Available online: www.geotomosoft.com (accessed on 14 August 2018).
58. Gharibi, M.; Bentley, L.R. Resolution of 3-D Electrical Resistivity Images from Inversions of 2-D Orthogonal Lines. *J. Environ. Eng. Geophys.* **2005**, *10*, 339–349. [[CrossRef](#)]
59. Berge, M.A.; Drahor, M.G. Electrical Resistivity Tomography Investigations of Multilayered Archaeological Settlements: Part II—A Case from Old Smyrna Höyük, Turkey. *Archaeol. Prospect.* **2011**, *18*, 291–302. [[CrossRef](#)]
60. Rödder, T.; Kneisel, C. Permafrost mapping using quasi-3D resistivity imaging, Murtèl, Swiss Alps. *Near Surf. Geophys.* **2012**, *10*, 117–127. [[CrossRef](#)]
61. Schwindt, D.; Kneisel, C. Optimisation of quasi-3D electrical resistivity imaging—Application and inversion for investigating heterogeneous mountain permafrost. *Cryosphere Discuss.* **2011**, *5*, 3383–3421.

62. Papadopoulos, N.G.; Tsourlos, P.; Tsokas, G.N.; Sarris, A. Two-dimensional and three-dimensional resistivity imaging in archaeological site investigation. *Archaeol. Prospect.* **2006**, *13*, 163–181. [[CrossRef](#)]
63. Dahlin, T.; Zhou, B. A numerical comparison of 2D resistivity imaging with ten electrode arrays. *Geophys. Prospect.* **2004**, *52*, 379–398. [[CrossRef](#)]
64. Loke, M.; Dahlin, T. Methods to Reduce Banding Effects in 3-D Resistivity Inversion. In Proceedings of the Near Surface 2010—16th EAGE European Meeting of Environmental and Engineering Geophysics, Zurich, Switzerland, 6–8 September 2010. [[CrossRef](#)]
65. Tejero-Andrade, A.; Cifuentes, G.; Chávez, R.E.; López-González, A.E.; Delgado-Solórzano, C. L- and CORNER-arrays for 3D electric resistivity tomography: An alternative for geophysical surveys in urban zones. *Near Surf. Geophys.* **2015**, *13*, 355–368. [[CrossRef](#)]
66. Bobachev, A.; Modin, I.; Shevinin, V. *IPI2Win V2.0: User's Guide*; Moscow State University: Moscow, Russia, 2003; Available online: <http://geophys.geol.msu.ru/ipi2win.htm> (accessed on 10 January 2003).
67. Koefoed, O. *Geosounding Principles 1: Resistivity Sounding Measurements*; Elsevier Science Publishing Company: Amsterdam, The Netherlands, 1979.
68. Van Overmeeren, R.A. Aquifer boundaries explored by geoelectrical measurements in the coastal plain of Yemen: A case of equivalence. *Geophysics* **1989**, *54*, 38–48. [[CrossRef](#)]
69. Loke, M.H.; Barker, R.D. Rapid least-squares inversion of apparent resistivity pseudosections by a quasi-Newton method. *Geophys. Prosp.* **1996**, *44*, 131–152. [[CrossRef](#)]
70. Loke, M.H. Tutorial: 2D and 3D Electrical Imaging Surveys. 2020. Available online: <http://www.geotomosoft.com/downloads.php> (accessed on 7 August 2020).
71. Farquharson, C.G. Constructing piecewise-constant models in multidimensional minimum structure inversions. *Geophysics* **2008**, *73*, K1–K9. [[CrossRef](#)]
72. Geosoft. *Oasis Montaj 8.3. Mapping and Application System*; N5SIV6. Users' Manual; Geosoft Inc.: West Toronto, ON, Canada, 2015; Available online: <https://www.geosoft.com/products/oasis-montaj> (accessed on 22 October 2018).
73. Auken, E.; Foged, N.; Sørensen, K.I. Model Recognition by 1-D Laterally Constrained Inversion of Resistivity Data. In Proceedings of the 9th Meeting, Environmental and Engineering Geophysical Society—European Section, Prague, Czech Republic, 8 September 2002; pp. 241–244. [[CrossRef](#)]
74. Brissaud, A.; Desbordes, C. Bulletin de la Société Française des Fouilles de Tanis. Activity Report—2018 Campaign, MATD, Mission of Archaeology at Tell Dibgou, No 32, 21P. 2018. Available online: <http://www.telldibgou.fr/index.php/rapports-d-activite/2018> (accessed on 1 February 2019).
75. Dahlin, T.; Loke, M.H. Quasi-3D resistivity imaging-mapping of three dimensional structures using two dimensional DC resistivity techniques. In Proceedings of the 3rd EEGS Meeting; European Association of Geoscientists & Engineers, Houten, The Netherlands, 11–13 August 1997; pp. 143–146.
76. Salem, A.; Williams, S.; Fairhead, J.; Ravat, D.; Smith, R. Tilt-depth method: A simple depth estimation method using first-order magnetic derivatives. *Lead. Edge* **2007**, *26*, 1502–1505. [[CrossRef](#)]
77. Cooper, G.R.J.; Cowan, D.R. Enhancing potential field data using filters based on the local phase. *Comput. Geosci.* **2006**, *32*, 1585–1591. [[CrossRef](#)]
78. Cooper, G.R.J.; Cowan, D.R. Edge enhancement of potential-field data using normalized statistics. *Geophysics* **2008**, *73*, 1–4. [[CrossRef](#)]
79. Cooper, G.R.J. Balancing images of potential field data. *Geophysics* **2009**, *74*, 17–20. [[CrossRef](#)]